






# Chapter 4

## Simulation and Modeling of Direct Gas Injection through Poppet-type Outwardly-opening Injectors in Internal Combustion Engines



Abhishek Y. Deshmukh , Mathis Bode, Tobias Falkenstein ,  
Maziar Khosravi , David van Bebbber, Michael Klaas ,  
Wolfgang Schröder and Heinz Pitsch 

**Abstract** The obligation for the development of highly efficient and low-emission combustion engines has renewed interest in compressed natural gas (CNG) engines using a direct injection (DI) system. CNG has high knock resistance, and with the use of DI, the volumetric efficiency can be increased compared to port-injected CNG engines. Additionally, carbon dioxide and particulate emissions are lower due to a high hydrogen-to-carbon ratio. Therefore, the DI-CNG technology has the potential to surpass the thermal efficiency of conventional gasoline spark-ignition

---

A. Y. Deshmukh (✉) · M. Bode · T. Falkenstein · H. Pitsch  
Institute for Combustion Technology, RWTH Aachen University,  
Templergraben 64, 52062 Aachen, Germany  
e-mail: [a.deshmukh@itv.rwth-aachen.de](mailto:a.deshmukh@itv.rwth-aachen.de)

M. Bode  
e-mail: [m.bode@itv.rwth-aachen.de](mailto:m.bode@itv.rwth-aachen.de)

T. Falkenstein  
e-mail: [t.falkenstein@itv.rwth-aachen.de](mailto:t.falkenstein@itv.rwth-aachen.de)

H. Pitsch  
e-mail: [h.pitsch@itv.rwth-aachen.de](mailto:h.pitsch@itv.rwth-aachen.de)

M. Khosravi · D. van Bebbber  
Ford Research and Advanced Engineering, Ford Werke GmbH,  
Henry-Ford Str. 1, 50725 Cologne, Germany  
e-mail: [maziar.k@gmail.com](mailto:maziar.k@gmail.com)

D. van Bebbber  
e-mail: [dvanbebb@ford.com](mailto:dvanbebb@ford.com)

M. Klaas · W. Schröder  
Institute of Aerodynamics, RWTH Aachen University,  
Wüllnerstr. 5a, 52062 Aachen, Germany  
e-mail: [m.klaas@aia.rwth-aachen.de](mailto:m.klaas@aia.rwth-aachen.de)

W. Schröder  
e-mail: [office@aia.rwth-aachen.de](mailto:office@aia.rwth-aachen.de)

engines while producing lower emissions. However, the design of DI-CNG engines is challenging because of gaseous and, hence, highly compressible fuel running through small injector passages, which results in complex supersonic flows with shocks. The supersonic gas jets emerging from the injector outlet interact with the in-cylinder flow field, which has an impact on fuel–air mixing and combustion. Therefore, it is essential to understand the fundamental physics of the injection process to develop modeling strategies for DI-CNG systems and further study the influence of direct gas injection on the in-cylinder flow field and mixing. To this end, the current chapter is dedicated to the fundamental understanding of the gas injection process through poppet-type outwardly-opening injectors. The DI modeling strategies are discussed for the application in engine simulations. Furthermore, the impact of gas injection on the in-cylinder flow field and fuel–air mixing is analyzed for centrally-mounted injector configurations.

**Keywords** Compressed natural gas · Direct injection · Poppet-type outwardly-opening injector · Supersonic flow · Shocks · Modeling

## 4.1 Introduction

Internal combustion engines (ICEs) are currently the primary power source for ground transportation and will continue to power, at least, heavy-duty vehicles and off-road applications in the future (Eilts 2016). With increasing restrictions on emissions for the transportation sector, research and development efforts must be directed toward significantly reducing engine-out emissions and improvement of the overall efficiency of ICEs through several viable options such as efficient combustion, exhaust after-treatment, or use of low carbon fuels. Compressed natural gas (CNG) is a highly attractive alternative low carbon fuel with high hydrogen-to-carbon ratio and has a potential for efficient combustion.

### 4.1.1 Direct Gas Injection

CNG engines with port fuel injection (PFI) technology have existed for a long time. However, CNG engines have not fully exploited their potential because of some limitations of PFI technology, e.g., reduced drivability and potential methane slip. The reason for reduced drivability of a PFI-CNG vehicle is lower part-load torque compared with gasoline or diesel ICEs, which is caused by the reduction in volumetric efficiency due to the displacement of air as CNG is injected into the manifold. Furthermore, during the valve overlap period, the unburnt methane–air mixture may be passed directly to the exhaust ports resulting in methane slip. The direct injection (DI) of CNG into the cylinder shows the potential to outperform PFI (Husted et al. 2014). Recent work, e.g., the InGas Collaborative Project (INGAS 2017), focused on the development of innovative technologies for CNG engines

such as operating PFI and DI engines under stoichiometric and lean burn conditions to improve efficiency. The present focus, e.g., within the GasOn project by the European Council for Automotive Research & Development (EUCAR) (European Council for Automotive R&D 2018), is to develop CNG-only engines to achieve stricter emission targets.

Despite clear advantages, DI-CNG engines are not predominantly used so far because of the challenges in their design and development. The main challenges in the design process come from the direct gaseous fuel injection, which appears simpler than liquid fuel injection, but is, in fact, a complex process because of the compressible nature of the gas (Müller et al. 2013) and small complex geometries of the injector nozzles. The gas flowing through the injector nozzle with changing area of cross section accelerates to supersonic speeds if the pressure ratios across the nozzle exceed critical values (typically 2–2.5). Moreover, the effects of gas injection on well-established design strategies for conventional ICEs are not well understood. For example, the intake ports of conventional SI engines are optimized to generate a strong tumble vortex in the cylinder. The tumble vortex accelerates by spin-up effect and breaks into a large number of smaller eddies by piston compression, which results in high turbulence near ignition timing, leading to faster combustion (Arcoumanis et al. 1990; He et al. 2007). On the other hand, in a compression ignition (CI) engine, a swirling flow field is desired and generated by the swirl intake ports to aid mixing and diffusion-controlled combustion of the injected fuel by enhancing oxidizer entrainment (Fuchs and Rutland 1998; McCracken and Abraham 2001). Regardless of the potential application of direct gas injection, either in an SI or in a CI engine, e.g., in a dual-fuel application, the high-momentum gas jet strongly affects the in-cylinder flow field and mixing (Chiodi et al. 2006; Baratta et al. 2017; Sevik et al. 2016). Therefore, it is crucial to fundamentally understand the process of gas injection and its consequences on the overall engine performance with existing engine designs, which will then help to devise new design strategies for DI-CNG engines. However, the experimental investigations of the nozzle flow and the near-nozzle gas jet are difficult due to small injector geometries and very small flow timescales. Furthermore, the injected gas jet is highly fluctuating and dynamically interacts with the in-cylinder flow field, making it difficult to measure the velocity field and mixing experimentally. Therefore, predictive simulations are integral to the design and development of DI-CNG systems. A first step toward the understanding of the direct gas injection is to perform resolved simulations of the injector nozzle flow, near-nozzle flow, far-field development of the gas jet in order to characterize the gas jet behavior of DI-CNG injectors in detail.

### ***4.1.2 Design Considerations for Direct Gas Injector***

From a practical point of view, the design and development of the direct gas injector require several considerations as studied by Husted et al. (2014). As

opposed to injectors for liquid fuels, the gas injector lacks lubrication by the fuel, requiring additional means of lubrication to extend the durability. Additionally, a high mass flow rate is desired to inject a sufficient amount of gas in each engine cycle depending on the operation condition. For higher mass flow rate, either the flow area needs to be large or the injection pressure must be high. High pressure also promotes mixing, but on the other hand, to maximize the vehicle range, lower injection pressure is required so that the maximum amount of CNG can be obtained from the pressurized tank before the tank pressure falls below the desired injection pressure. It should be noted that the current design assumption of CNG engines omits the use of high-pressure fuel pump as used in DI gasoline and diesel applications. For example, current PFI systems use injection pressure of around 8 bar and can use more than 96% of CNG from the tank. Using the same injection pressure in the DI system would significantly limit the peak power of the engine or put too many constraints on the design of the injector. Increasing injection pressure to 15 bar will reduce the vehicle range by  $\sim 3\%$ , and a further increase of injection pressure to 30 bar will decrease the vehicle range by  $\sim 9\%$ . Therefore, for a chosen CNG direct injector, the optimum injection pressure is a trade-off between the engine output at the desired operating conditions and the vehicle range. The trade-off can be shifted favorably by careful design of the injector nozzle by maximizing the flow area.

There are mainly three types of injector designs currently used, namely an inwardly-opening needle with a multi-hole tip for diesel, an inwardly opening needle with counterbore cylindrical holes for gasoline direct injection (GDI), and an outwardly-opening poppet-type needle for GDI applications. The selection of the injector nozzle design for DI-CNG applications is primarily driven by the pressure difference across the nozzle in the operating range. In diesel or GDI engines, the injection pressure ( $>100$  bar) is much higher than the peak cylinder pressures during the entire engine cycle, whereas it is significantly lower in DI-CNG ( $<20$  bar) to achieve maximum vehicle range as described before. Therefore, inwardly opening DI-CNG injectors could be inadvertently opened at high in-cylinder pressures. On the other hand, the outwardly-opening poppet-type valves are sealed by the cylinder pressure (see Fig. 4.1), and therefore, the outwardly-opening poppet-type valves have become a natural choice for DI-CNG applications.

### ***4.1.3 Flow Through Poppet-Type/Outwardly Opening Injectors***

The nozzle geometry of outwardly opening poppet-type injectors (henceforth called poppet-type injectors) is complex, and compressible gas flow through the small and complex passages can be rich in physical phenomena. Compared to cylindrical nozzles, there have been relatively a few experimental and simulation studies of outwardly opening poppet-type nozzle designs in the literature. Kim et al. (2004)

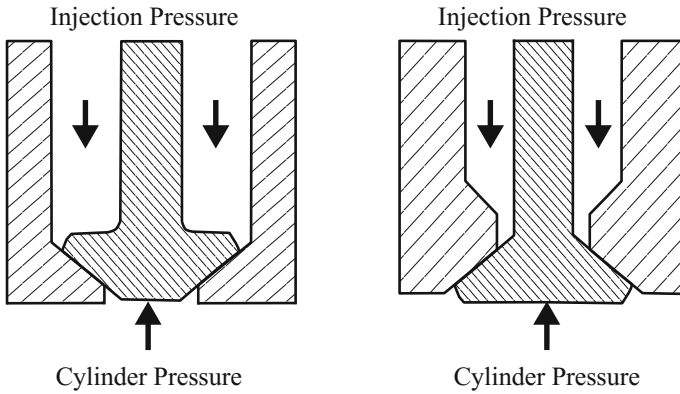


**Fig. 4.1** Schematic of design of inwardly (*left*) and outwardly (*right*) opening injector nozzles

carried out URANS simulations of direct natural gas (NG) injection through shrouded and unshrouded poppet-type nozzle geometries in a large bore, low-speed two-stroke ICE. At lower injection pressure ( $\sim 4$  bar), the injection resulted in a collapsed gas jet, whereas at higher pressure ( $\sim 35$  bar) the gas jet did not collapse, but instead attached to the walls of the cylinder head resulting in a Coanda-type flow. With the use of a shrouded poppet-type nozzle, the gas jet was forced to collapse at higher pressure. The authors also analyzed the effect of these nozzle designs on the mixing performance, combustion efficiency, and susceptibility to pollutant formation and found that high injection pressure with shrouded nozzle resulted in a higher flammability of the mixture. Baratta et al. (2011) showed for a poppet-type injector that the wave propagation inside the injector and the needle motion affect the mass flow rate and the resulting gas jet before collapsing. They suggested the use of fixed needle lift with a ramp of injection pressure to mimic the effects of needle opening. Kuensch et al. (2014) studied a far-field gas jet development in a constant pressure chamber emerging from a piezoelectrically actuated poppet-type injector. They used a planar laser-induced fluorescence (PLIF) technique with acetone as a tracer to track the injected nitrogen gas in the chamber filled with air. The temporal development of the gas jet was visualized, which showed a two-stage gas jet evolution. In the first stage, a hollow cone was formed, which, in the second stage, collapsed into a single jet penetrating the chamber along the axial direction. It was observed that the injection pressures and needle lifts controlled the collapsing tendency of the hollow cone, with higher injection pressure and needle lift lowering the collapsing tendency.

Keskinen et al. (2016) carried out URANS simulations to investigate the gas jet from a cylindrical as well as a poppet-type nozzle. They compared different turbulence models and observed that the jet tip penetration was overpredicted by the RNG  $k-\epsilon$  model, whereas the quadratic  $k-\epsilon$  model resulted in a better agreement with the experimental data. Therefore, the quadratic  $k-\epsilon$  model was chosen for further DI engine simulations. The results showed different mixing mechanisms for

different nozzle designs. The gas jet from the poppet-type nozzle predominantly showed free jet mixing, whereas the cylindrical nozzle favored the mixing induced by impingement of the jet on the piston. As a consequence, a faster mixing was observed with the poppet-type nozzle for early injection timing, while, for late injection timing, the cylindrical nozzle resulted in faster mixing due to impingement of the gas jet on the piston top. Detailed X-ray radiography experiments were performed by Bartolucci et al. (2016) in a nitrogen-filled chamber using a poppet-type injector with nitrogen as the injected gas. The flow around the pintle of the nozzle and the subsequent gas jet development was investigated using the URANS simulations, and a good agreement was observed between simulations and experiments. A mesh resolution study was also carried out that suggested the use of fine mesh resolution for such simulations. However, a detailed upstream geometry of the injector except the pintle was unknown in this case, which is very important for accurate prediction of the development of the gas jet. Besides, with increasing mesh resolution, the computational cost increases significantly. Therefore, to reduce the computational expenses, some modeling approaches to replace poppet-type injectors have been suggested in the literature, e.g., a converging–diverging nozzle approximation for a shrouded poppet-type valve by Kim et al. (2007), a source modeling approach by Baratta et al. (2011), and a mapped boundary condition (MBC) approach by Deshmukh et al. (2016).

So far, most studies using poppet-type injectors have focused on full engine URANS simulations including either fully resolved simulations of the injectors or models of the injectors to overcome computational challenges. The turbulence models have been used in these simulations with little validation against higher fidelity methods such as LES. Provided a sufficient mesh resolution is used, an accurate time-resolved flow field can be obtained using a high-fidelity LES. Along with turbulent mixing characteristics, the classical features of high Mach flows can also be observed for poppet-type injectors, e.g., annular Mach disks and barrel shocks. Furthermore, the effects of the initial condition and needle motion are reported to be very important but have not been quantified in terms of jet characteristics.

#### **4.1.4 Scope**

This chapter aims to introduce the reader to a systematic characterization of the gas jet emerging from a poppet-type injector using LES, which may further provide insights into the fundamental physical processes and the effects. The LES simulations are used to characterize the nozzle flow, near-nozzle gas jet, and the far-field gas jet in detail. A few turbulence models are compared against the LES, and a possible choice for URANS is suggested. The effects of initial conditions in the nozzle and the needle motion are discussed, and recommendations for further engine simulations are provided. The modeling approaches for poppet-type injectors are discussed in detail. The recent MBC modeling approach is then

demonstrated for *quasi*-steady and engine configurations. The idea is to provide comprehensive simulation and modeling approaches of the chosen poppet-type injector used for DI-CNG application in ICEs.

In the following, resolved numerical simulations of the poppet-type injector using both LES and URANS methods are discussed in Sect. 4.2. The challenges in the use of a resolved simulation approach in real engine applications are described, which motivate the development of models for injector nozzles. Previously developed models are discussed briefly in Sect. 4.3. The recently developed MBC approach is applied to quasi-steady-state and full engine configurations, and the results are discussed in Sect. 4.4. The impact of direct gas injection on the in-cylinder flow and mixing is discussed in Sect. 4.5. The chapter is summarized in Sect. 4.6, and future challenges are discussed in Sect. 4.7.

## 4.2 Simulations of Gas Injection Through Poppet-Type Injectors: A Case Study

### 4.2.1 Numerical Challenges

From a numerical point of view, resolved simulations of the poppet-type injector are challenging because of small and complex gas passages of the order of micrometers and high-speed flow with shocks and discontinuities typical in supersonic regimes. LES provides a feasible approach to obtain highly accurate flow field simulations in complex industrial geometries. Especially for flows with high Mach numbers and Reynolds numbers, where the computational cost of DNS is high, LES can be a practical alternative. LES of flows with shocks requires special numerical schemes with the capability to capture shocks and remain stable at the same time. The numerical stability can be obtained by adding numerical dissipation. However, this must be limited to areas of shocks and discontinuities to avoid dissipation of physical turbulent flow structures. A shock detector is required to add numerical dissipation just locally and conserve turbulent flow structures. The shock detector determines gradients in the velocity and scalar field and activates the shock-capturing scheme in the regions of high gradients. In addition, supersonic velocities in combination with grid cell sizes of the order of micrometers result in time steps on the order of 100 picoseconds. A high-fidelity full engine LES simulation with a fully resolved gas injector simulation may need years to complete one or more cycles. Nevertheless, a fully resolved LES of the gas jet from the injector is still feasible for a simplified case, such as a constant pressure or constant volume chamber because the run-times are shorter due to the reduced domain of interest compared to full engine simulations.

On the other hand, URANS simulations may be computationally cheaper due to lower mesh resolution requirements compared to LES. However, since the energy-containing turbulent scales are also modeled, the accuracy of the solution

needs to be carefully evaluated. Also, most of the turbulence models for URANS have been developed for specific applications and may generally not be applied to direct gas injection studies. Nevertheless, the turbulence models are extensively used in industry for different applications including direct gas injection. The URANS approach is very dissipative as it adds a high amount of eddy viscosity to the molecular viscosity, and therefore, central difference numerical schemes may remain stable in the presence of shocks. However, a drawback is that the shocks and discontinuities are dissipated quickly and do not survive for longer times.

## 4.2.2 Case Description

Recently, Deshmukh et al. (2018a, b) performed LES of a helium gas jet from a poppet-type injector in a closed chamber to obtain an accurate time-resolved flow field along with turbulent mixing characteristics. This is considered as a case study here to understand physical and numerical aspects in the simulation of gas injection through poppet-type injectors. First, the nozzle flow and near-nozzle gas jet development are discussed, and then, the far-field jet evolution is validated with the experimental data.

**Experimental Data.** Delphi has developed a fourth-generation electromagnetically actuated solenoid injector for DI-CNG applications (Husted et al. 2014). It is an outwardly opening poppet-type injector. A helium gas jet through the injector was characterized experimentally at Delphi. The schematic of the experimental setup is shown in Fig. 4.2. Helium at a pressure of 16 bar and ambient temperature was injected into the ambient air, and the Schlieren imaging technique, which can capture density gradients in a flow field, was used to visualize the temporal evolution of the gas jet. The selection of helium in this study was driven by the consideration that the Schlieren measurement technique requires high gradients in the density field to work well. This study aimed to investigate the fundamental physical processes behind the hollow-cone gas jet formation and the characterization in terms of global parameters.

**Simulation Methods.** The state-of-the-art compressible solver Compressible High-speed Reactive Solver (CHRIS), which is developed by Cascade Technologies Inc., is used for high-fidelity LES (Brès et al. 2012). CHRIS uses an unstructured mesh to solve the compressible Navier–Stokes equations along with scalars in the conservative form using a novel low-dissipation and low-dispersion finite volume method (Khalighi et al. 2011). A third-order total variation diminishing (TVD) Runge–Kutta scheme is used to explicitly solve the equations in time (Shu and Osher 1988). The essentially non-oscillatory (ENO) scheme (Shu and Osher 1988) is used together with a shock detector to capture shocks and discontinuities. Shock detectors based on the normalized flow solution and based on the absolute pressure dilatation are available in CHRIS. The ENO scheme is used in the regions of shocks identified by a shock detector to ensure the stability of the



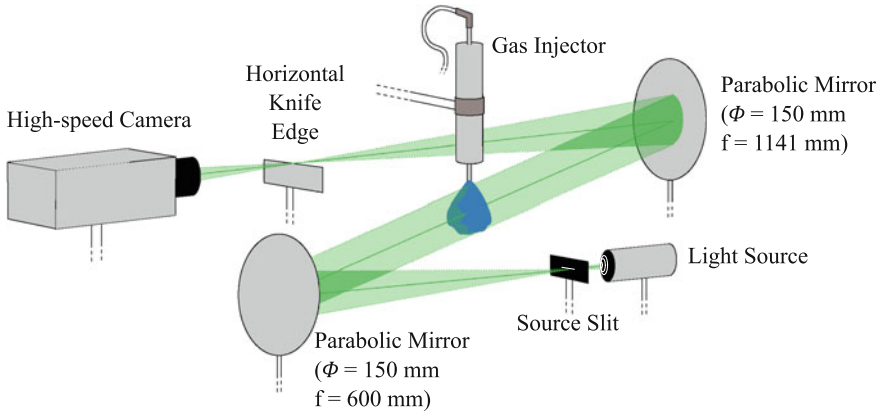


**Fig. 4.2** Schematic of the experimental setup at Delphi

numerical scheme by adding local numerical dissipation. The energy-containing turbulent structures are resolved by the low-dissipation scheme away from the shocks, and sub-filter scales are modeled using the Vreman model (Vreman et al. 1995). The ideal gas (IG) equation of state (EOS) is used to calculate pressure from temperature and density. For detailed governing equations and used parameters, the reader is referred to Deshmukh et al. (2018a).

For URANS simulations, the commercial Computational Fluid Dynamics (CFD) code CONVERGE (version 2.3.9) by Convergent Science Inc. (Richards et al. 2016) is used. CONVERGE is a compressible 3D flow solver, specifically developed for the computation of steady-state or transient flows in complex and moving geometries. In this study, a spatially second-order central difference numerical scheme was selected. A first-order Euler backward scheme is used to solve the equations in time, which results in fully implicit time integration. The pressure is calculated from density and temperature using the Redlich-Kwong (RK) EOS. The system of equations is solved using a modified pressure implicit with splitting operators (PISO) algorithm. For detailed equations and used numerical schemes, the reader is referred to the CONVERGE manual (Richards et al. 2016), whereas for details on parameters used in this study the reader is referred to Deshmukh et al. (2018a).

*Equation of State.* The IG EOS is used in the LES, which is justified because the compressibility factors for the gases involved in the study, namely helium, nitrogen, and oxygen, do not significantly diverge from 1.0 in the relevant operating range (Van Sciver 2012; Jensen et al. 1980). On the other hand, the RK EOS, which follows real gas behavior, is chosen for the URANS simulations. The choice is motivated by the subsequent applicability of the results of the fundamental investigations to full engine simulations. A real gas EOS is required in URANS simulations of a full engine configuration because the in-cylinder pressure during an engine cycle varies in the range, where the real gas effects become significant.

Therefore, the RK EOS is used in the current setup. The compressibility factor of the in-cylinder gas mixture in the engine simulations reported in the next sections varied between 0.98 and 1.004. Nevertheless, the RK EOS should ideally approach the IG EOS under the conditions considered in this study. To verify that, a comparison of the density of helium computed with the IG EOS and RK EOS at injection pressure and ambient pressure for a relevant range of temperatures was performed. The relative error in density is less than 0.025%, which substantiates the presumed convergence of RK EOS toward IG EOS under the conditions relevant to this study.

**Simulation Setup.** A cylindrical domain with a diameter of 75 mm and a height of 82.5 mm, which are typical dimensions for a downsized engine cylinder of a passenger car, is used for the numerical simulations (see Fig. 4.3a). The injector is placed at the top, on the axis of this cylinder, but is not shown here. The meshes used in the simulations are shown on a representative plane ( $Y = 0.0$ ) through the domain.

The ANSYS Meshing software (ANSYS<sup>®</sup> Meshing 2013) is used to generate a hybrid mesh, which comprises stretched prism layers attached to the walls and hexagonal cells away from the walls. The hybrid mesh is used for LES and contains approximately 24 million cells. The mesh inside the injector nozzle contains 5 stretched prism layers with a stretching factor of 1.2 on each side at the wall and 10–20 hexagonal cells across the gaps between the prism layers. A highly refined mesh is generated near the nozzle exit, and the mesh size is gradually increased in a concentric manner away from the nozzle, which helps to capture the shocks and pressure waves traveling concentrically outward from the injector nozzle. The minimum and maximum cell sizes of hexagonal cells in the domain are approximately 18.75 and 600  $\mu\text{m}$ , respectively. The resulting downstream mesh is shown in Fig. 4.3b.

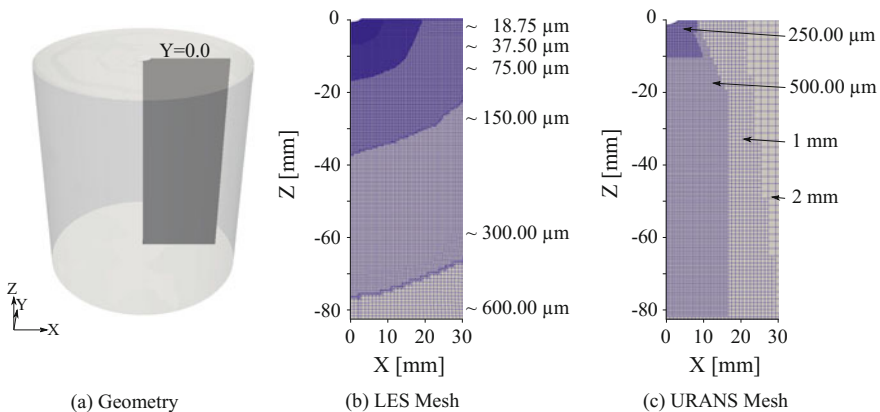


**Fig. 4.3** Computational domain and mesh for LES and URANS simulations depicted on a representative plane

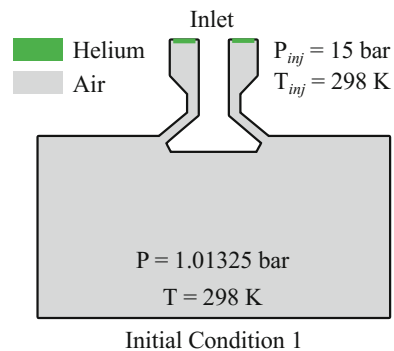
The mesh resolution study by Bartolucci et al. (2016) suggested the use of highly refined meshes for the gas jet URANS simulations. However, the computational costs for such resolutions can be intractable for practical engine simulations. Therefore, the mesh size in the URANS simulations is chosen such that it is directly applicable in the subsequent engine simulations. CONVERGE generates a Cartesian cut-cell mesh at run-time. The base size for the mesh is set to 2 mm. The near-nozzle and upstream region are refined using several successive embedded regions, which results in the smallest cell size of  $64.5 \mu\text{m}$  within the nozzle gaps (not shown here). CONVERGE has an adaptive mesh refinement (AMR) capability. However, for comparison with LES, which has a fixed mesh, the AMR is switched off in all URANS. The resulting mesh (see Fig. 4.3c) is used in all URANS simulations in this study.

A Courant–Friedrichs–Lewy (CFL) number of 1.0 is set in the LES, which is the limit for the used explicit third-order TVD Runge–Kutta scheme. In the URANS, an implicit solver is available, which allows a CFL of 2.0 to speed up the simulations. The results with a CFL of 1.0 in the URANS were not significantly different.

*Initial Conditions.* The initial conditions in the computational domain are shown schematically in Fig. 4.4. The injector needle is set in an open position with the needle lift of  $300 \mu\text{m}$ , which is fixed throughout the simulation and is less than the maximum lift of  $350 \mu\text{m}$ . The resulting mass flow rate in the LES is close to the measured mass flow ( $\sim 3.5 \text{ g/s}$ ) of helium through the injector. Initially, the domain is filled with air (77%  $\text{N}_2$  and 23%  $\text{O}_2$  by mass) at a pressure of 1.01325 bar and a temperature of 298 K, which is referred to as initial condition 1 (or briefly as IC1). The region is set to zero velocity.

*Boundary Conditions.* A total pressure of 15 bar, temperature of 298 K, and helium mass fraction of 1.0 are set at the inlet of the nozzle for all simulations. Remaining boundaries are treated as adiabatic, no-slip walls. Some differences between the simulation and experimental conditions must be noted; e.g., the injection pressure in experiments was maintained at 16 bar, although the predetermined operating pressure is 15 bar, which was used in simulations. Despite differences in the injection pressure and the needle lift, the mass flow rate in the simulations is slightly

**Fig. 4.4** Schematic diagram of initial condition 1



higher than the measured mass flow rate. The second difference is that the measurements were carried out in open ambient conditions, whereas the simulations were performed in a closed chamber. However, it has been shown that due to the short duration of injection of 700  $\mu\text{s}$ , these differences have insignificant effects on the intended study and conclusions (Deshmukh et al. 2018a).

The duration of injection (DOI) is fixed to 700  $\mu\text{s}$  for all simulations. During the injection period, the gas jet reaches close to the opposite boundary of the computational domain. Detailed qualitative and quantitative analyses of the nozzle flow, near-nozzle, and far-field gas jet are carried out using the data generated in LES and URANS simulations.

### 4.2.3 Nozzle Flow

The nozzle flow is one of the most critical processes of gas injection because the pressurized gas undergoes expansion in the nozzle and accelerates to supersonic speeds depending on the geometry of the nozzle. The geometry of the nozzle and the pressure ratio essentially determine the flow conditions at the nozzle exit. Further gas jet evolution depends on the flow properties at the nozzle exit. In the poppet-type injector nozzle, the gas passages frequently change the direction of the flow. Also, the gas flow, in general, encounters the converging and diverging sections (see Fig. 4.5). Such a geometric configuration with the higher than critical pressure ratio across the nozzle drives the gas flow to first sonic speeds and then to supersonic speeds. Because of changing direction, a boundary layer separation occurs within and at the exit of the nozzle and recirculation regions form. To capture these viscous effects, a no-slip boundary condition is applied at the nozzle walls. A schematic diagram of the nozzle flow and the initial development of the helium gas jet are shown in Fig. 4.5. To analyze the nozzle flow, five locations are chosen considering the axisymmetric geometry of the nozzle. These are location 1, which is near the inlet, location 2 in the converging section, location 3 approximately located at the throat, and location 4 corresponding to the nozzle exit, and the centerline of the nozzle gap.

Considering the geometrical symmetry about the axis and steady-state condition of the flow in the nozzle, a combined azimuthal and time-averaging (Farrace et al. 2015) is used to compute the averaged velocity profiles, and the statistical information is obtained. For the statistical independence of the samples in space and time, the integral length and timescales are estimated carefully (Deshmukh et al. 2018b), which resulted in the azimuthal angle of  $30^\circ$  with 12 planes for spatial averaging and a sampling frequency of 67 kHz for time-averaging. A total of 492 individual samples are used to obtain the averaged velocity profiles in the nozzle at different locations after a steady-state flow condition is reached. The resulting averaged velocity profiles and the individual samples are shown in Fig. 4.6. The symbols are an indicator of the mesh density at the given location. Close to the nozzle inlet, i.e., the location 1, the W-velocity shows a flat averaged velocity

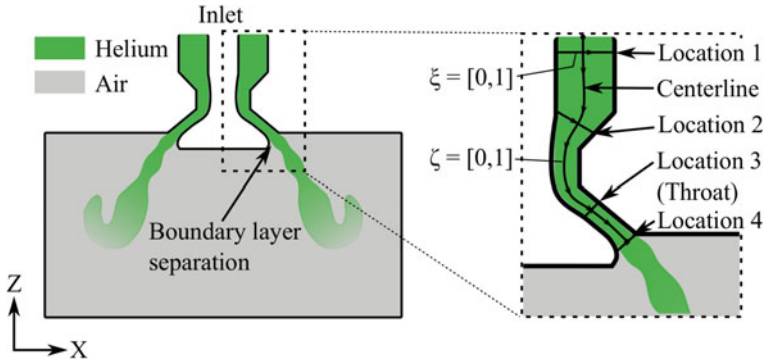


**Fig. 4.5** Schematic diagram for the analysis of nozzle flow

profile, whereas the other two components are almost zero. At location 2, substantial variation can be observed on the right boundary, which is because the flow speed increases in the converging section and the direction also changes, resulting in a recirculation region in the corner. At location 3, which is almost the throat section, the velocities reach sonic levels and further accelerate to supersonic levels as the gas passages diverge after the throat. A boundary layer separation occurs at location 4 as the boundaries diverge further near the exit, which can be seen in the velocity profiles. The flow separation on the poppet boundary causes the formation of a recirculating region resulting in highly varying velocity profiles.

The resolved turbulent kinetic energy (TKE) can be estimated from the individual velocity profiles at four locations. Figure 4.7 shows the resolved TKE at four locations with multiplying factors to visualize all plots on the same scale. As expected, the locations with high variability, i.e., location 2 and location 4, show high TKE near the boundaries. The local bulk Reynolds number and  $y^+$  at the first cell are calculated at the chosen locations. Maximum Reynolds number of 20,400 and maximum  $y^+$  value of 21 are observed at location 3, which is expected because the bulk velocities are high. At location 4, the  $y^+$  value is  $\sim 7$  and the Reynolds number is 16,211, which is lower due to reduced density and reduced bulk velocity as a result of flow separation.

The averaged steady-state profiles of Mach number, pressure, temperature, and density on the centerline of the nozzle passage are depicted in Fig. 4.8. As the nozzle passage acts as a converging–diverging nozzle, the gas accelerates to supersonic velocities with Mach numbers higher than 2.0 close to nozzle exit. After the throat, the continuously changing direction of the flow leads to an isentropic expansion fan on the poppet boundary and a nearly isentropic compression shock on the outer boundary. The compression shock is visible near the nozzle exit. Temperature and density decrease continuously along the centerline of the nozzle passage and increase at the compression shock but are still below the ambient conditions. The pressure at the nozzle exit is higher than the ambient pressure, which causes further expansion of the gas to the ambient conditions. Overall, the nozzle operates under moderately under-expanded conditions.

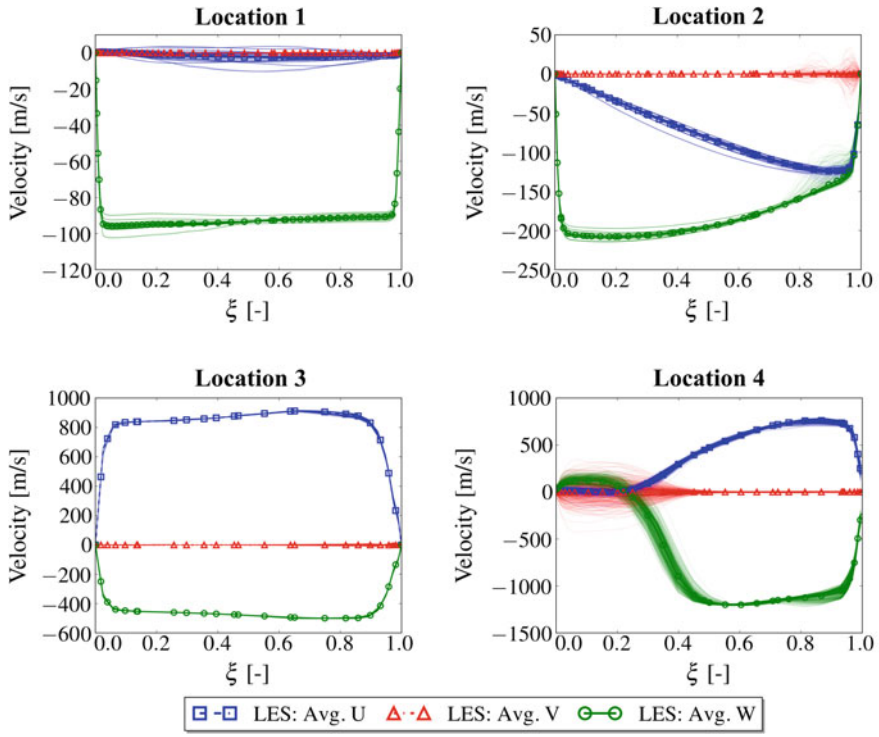


**Fig. 4.6** Steady-state velocity profiles at four chosen locations in the nozzle (*thin lines: individual profiles; thick lines: averaged profiles*)

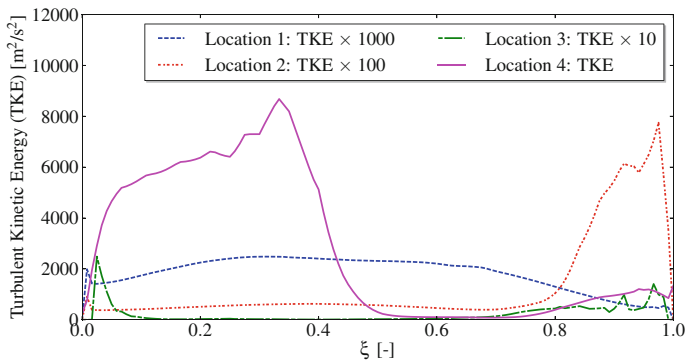


**Fig. 4.7** Resolved turbulent kinetic energy at four chosen locations in the nozzle

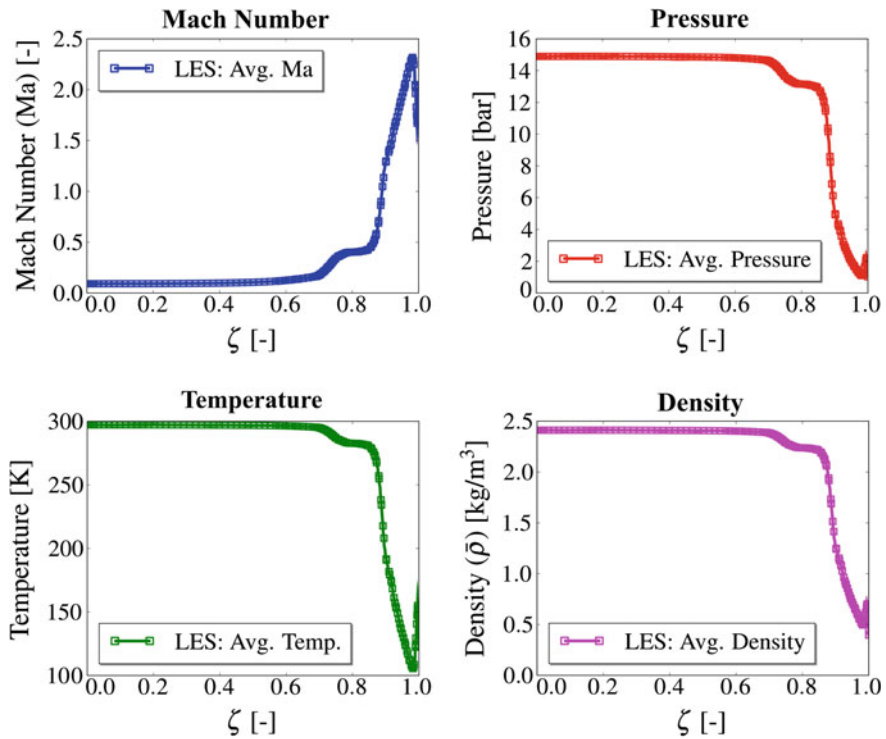


**Fig. 4.8** Averaged steady-state profiles of Mach number, pressure, temperature, and density on the centerline inside the nozzle (*inlet*:  $\zeta = 0.0$ ; *exit*:  $\zeta = 1.0$ )

#### 4.2.4 Near-Nozzle Gas Jet

The gas leaves the nozzle with supersonic velocity through the annular nozzle exit. Figure 4.9 shows a section through the domain at  $Y = 0.0$  depicting the very early phases of the development of the gas jets through contours of Mach number. The bow shocks can be seen clearly in the first frame. The annular bow shocks merge to form a complex interaction of waves behind the shock. The Mach disk and shock cells in the annular shape begin to form as a part of the hollow cone. The reflected shocks keep the hollow cone intact. Instabilities develop further downstream due to shear between helium and air, resulting in the formation of vortical structures similar to those in the wake of a bluff body. The initial bow shocks also interact with the gas jets during the early development phase, destabilizing them. The near-nozzle flow reaches steady state within  $60 \mu\text{s}$ .

Similar to the nozzle flow, a statistical characterization of near-nozzle jet formation can be performed. The near-nozzle jet statistics are computed using the combined azimuthal and time-averaging procedure described previously. The averaged steady-state velocity magnitude and the standard deviation for the jet are

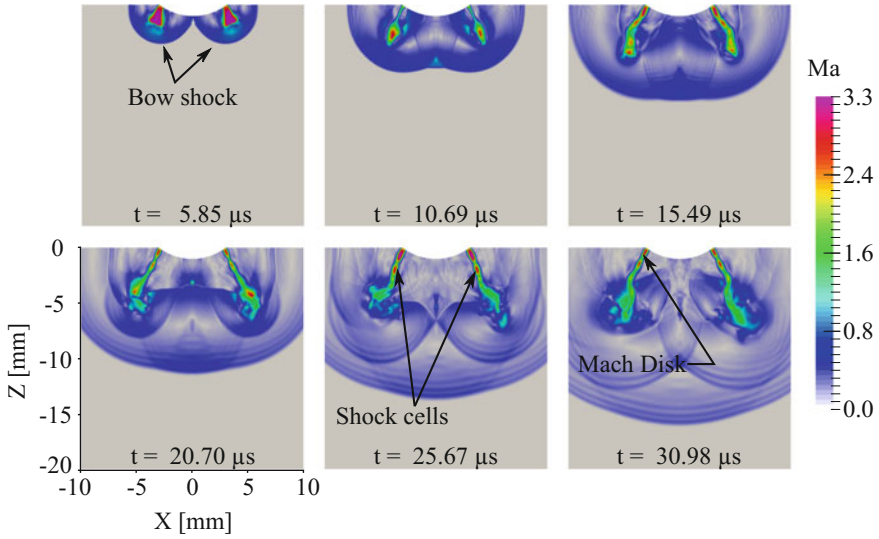


**Fig. 4.9** Initial development of the gas jet in terms of Mach number close to the nozzle exit and classical features of supersonic jets (*LES: Y = 0.0 plane*)

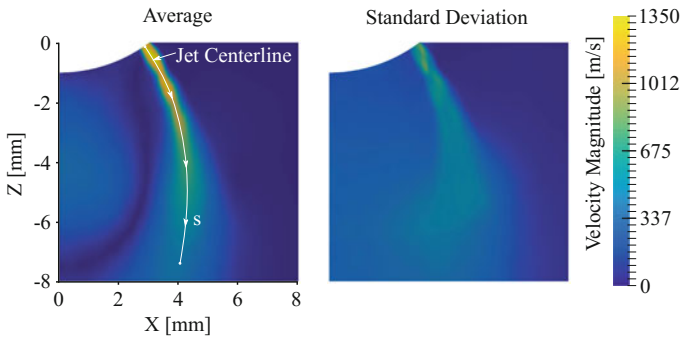


**Fig. 4.10** Near-nozzle steady-state averaged velocity magnitude and standard deviation in the LES

shown in Fig. 4.10. The near-nozzle mesh resolution used in this study cannot sharply resolve the typical structures of the supersonic gas jets. However, the formation of shock cells can be observed. As the pressure in the region below the poppet is low, the jet bends toward the axis of the injector. A highly fluctuating flow field near the nozzle results in the high standard deviation, particularly in the jet core near the nozzle exit. Nevertheless, the jet core mostly remains intact within the shock cells. The mixing of helium begins at the edges of the jet core, and mixing layers form on the inner edge and the outer edge (see Fig. 4.11). The thickness of both mixing layers gradually increases, and the two layers merge away from the



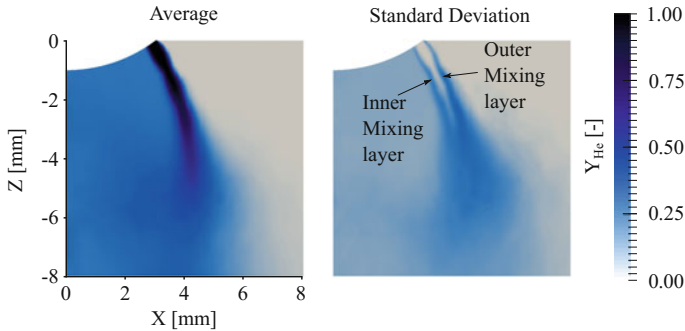


**Fig. 4.11** Near-nozzle steady-state helium mass fraction and standard deviation in the LES

nozzle exit. The helium–air mixture moves into the low-pressure region below the poppet, eventually increasing the helium concentration there.

The averaged steady-state profiles of different flow variables are plotted along the jet centerline in Fig. 4.12 along with the standard deviation ( $\sigma$ ) about the mean. The distance along the jet centerline is non-dimensionalized with the needle lift ( $L = 300 \mu\text{m}$ ) as a characteristic length scale. The average Mach number at the nozzle exit is approximately 2.0, and the average pressure is slightly above ambient. The helium expands into the ambient air, the average pressure drops, and the average Mach number increases up to  $\sim 2.6$ . After that, the pressure recovers and exceeds ambient pressure, and the Mach number drops. The cycle repeats until a distance of  $\sim 12$  times the needle lift. After initial fluctuations in the shock cells, the temperature remains stable at  $\sim 200 \text{ K}$  before the average Mach number drops below 1.0. Thereafter, the temperature begins recovering toward ambient conditions. The standard deviations of Mach number and pressure do not change significantly, although the absolute values are quite high. On the other hand, the standard deviation of density increases continuously, indicating mixing of helium with air, and the standard deviation of temperature first increases and begins decreasing after a distance of  $\sim 12$  times the needle lift. The average temperature in the near-nozzle gas jet is very low compared to ambient conditions.

### 4.2.5 Far-Field Gas Jet Evolution

The far-field gas jet development was analyzed using both experimental measurements and simulation data. The top row in Fig. 4.13 shows the visualization from the Schlieren experiments, while an isosurface corresponding to helium mass fraction of 0.003 from the LES is shown in the bottom row for the same instants as those of the experiments for direct comparison. The time shown here is relative to the instant when the gas jet first emerges from the injector.

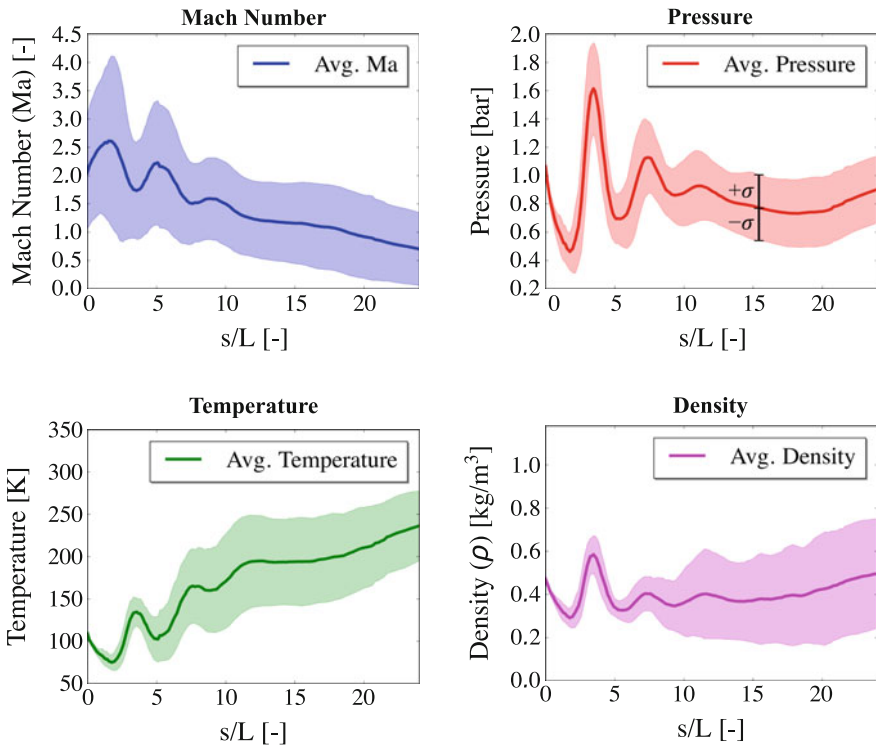


**Fig. 4.12** Near-nozzle steady-state profiles of Mach number, pressure, temperature, and density along the centerline of the gas jet

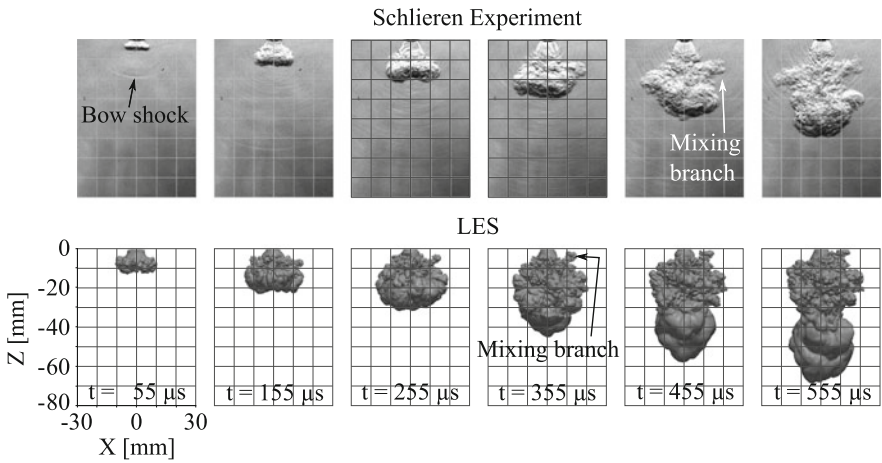


**Fig. 4.13** Comparison of the temporal development of the gas jet in Schlieren experiment (top row) and LES (bottom row: isosurface of  $Y_{\text{He}} = 0.003$ )

The initial bow shock is visible in the first and second Schlieren frame, and the pressure waves emitted from the jet are seen in the later frames. The gas jet continuously mixes with the ambient gas forming a cloud-like structure. A similar development can also be observed in the corresponding LES time frames. The range of length scales of the flow features observed in the experiments is qualitatively represented in the LES. The mixing branches of the gas jet moving in the transverse direction can be found in the experiment as well as the LES. The gas jet penetration in the experiments is shorter than in the LES. The reasons for the overprediction are the assumption of a fixed needle lift in the simulations and will be discussed later. However, a detailed view of the near-nozzle flow features is not available in the experimental data presented here.

From the simulation data, information on the mixing of the gas jet with surrounding gas can be obtained. For example, Fig. 4.14 shows the contours of the helium mass fraction at different time instants. As the gas jet develops, a hollow cone is formed initially. The high-speed gas flow entrains the surrounding gas, both from inside and from outside of the cone, which causes a pressure drop inside the cone below the poppet leading to the collapse of the hollow cone and formation of the single gas jet. It is possible to detect the collapsing event by monitoring the pressure below the poppet during the injection. The instantaneous pressure as shown in Fig. 4.15 is highly fluctuating, and a clear trend is not visible. Therefore, it is filtered to remove high-frequency oscillations. The filtered pressure values decrease after  $\sim 255 \mu\text{s}$  and fluctuate around lower levels when the hollow cone collapses.

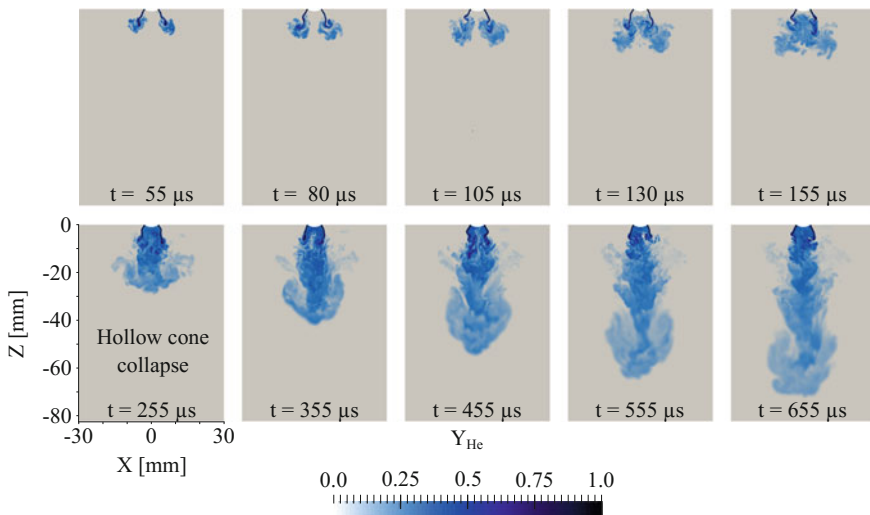


**Fig. 4.14** Development of the gas jet and mixing behavior as observed in  $Y = 0$  plane

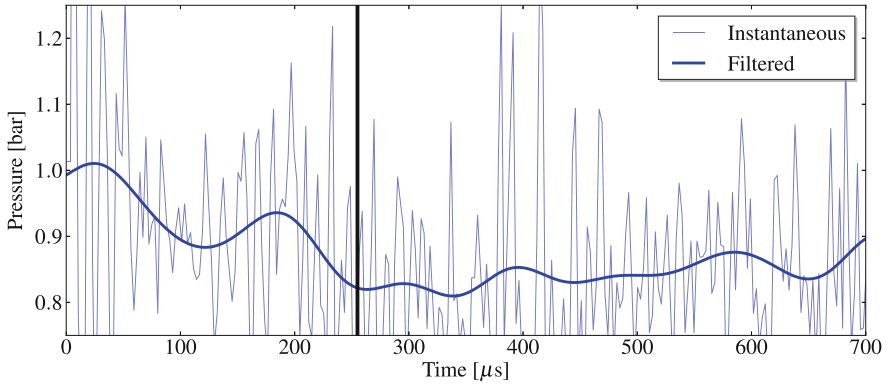


**Fig. 4.15** Pressure monitor below the poppet in LES; vertical black line  $t = 255 \mu\text{s}$  denotes the time of hollow-cone collapse

The far-field gas jet development and mixing can be characterized quantitatively in terms of different parameters, which are commonly used in the literature for liquid or gaseous fuel jets. These are:

- Axial penetration length (APL)
- Maximum width (MW)
- Area of the jet (AJ)
- Volume of the jet (VJ)
- Mass-weighted probability density function (PDF) of helium mass fraction within the volume of jet

Some of the parameters, such as axial penetration length, maximum width, and area of the jet, can be obtained from the experimental data, which are Schlieren images in this case. The Schlieren images are first converted into a binary image as shown in Fig. 4.16a ( $t = 455 \mu\text{s}$ ) using common image processing techniques. On the other hand, the simulations can provide information on additional parameters such as the volume of the jet and mixing statistics (see Fig. 4.16b, c, d) and help in gaining further insights into the mixture formation. The axial penetration length and maximum width provide spatial extents of the gas jet within the domain, while the area of the jet and the volume of the jet can be an indicator of the amount of entrainment of ambient gas. The mixing statistics determine the mixture quality and can establish the flammability limits of the mixture in a typical partially premixed combustion case. To compute the mixing statistics, one can either use normalized cumulative volume fraction plotted versus equivalence ratio (Sukumaran 2010) or compute mass-weighted PDF of the mass fraction of the injected gas within the jet volume (Vuorinen et al. 2014). The first method is preferable for full engine cases as the volume is fixed by walls of the combustion chamber, while the second method is appropriate for the free gas jets.

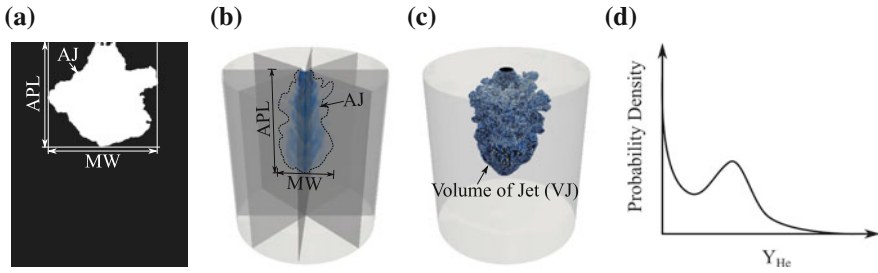


**Fig. 4.16** Methods of calculation of characterizing parameters from experiments (a) and simulations (b, c, d)

In the simulations, the characterizing parameters are computed from the computational domain using a threshold for the mass fraction of helium. The threshold value is selected based on the convergence of the parameters. In this study, the threshold value of 0.001 was found to be sufficient (Deshmukh et al. 2018a). The volume of the jet is computed by adding all cell volumes with helium mass fraction above the chosen threshold. The length of the bounding box of the jet volume along the axis of the jet constitutes the axial penetration length. The lateral penetration of the gas jet is different in different directions, and thus, the maximum width and the area of the jet depend on the plane of computation. Therefore, in this study, 24 planes with an angle of  $7.5^\circ$  between each other are selected passing through the axis of the cylindrical domain to calculate the maximum width and the area of the jet. As a result, a range of values is obtained for these parameters at a particular instant in time. It is important to note that different path lengths in the transverse direction are not the effect of directional sensitivity to the underlying Cartesian mesh. The mass-weighted PDF of helium mass fraction is computed from the volume of the jet. The statistical information such as mean, standard deviation, and skewness can be calculated from the PDF over time.

Figure 4.17 shows the comparison of all quantitative parameters from the LES with some of the available measured values. The axial penetration length is over-predicted in the simulations, although the slope of the line matches at later times. A nonlinear behavior is predicted in the initial phases of the jet development, which results in higher axial penetration in the beginning. Similar nonlinear behavior was observed in the experimental studies of the hollow-cone gas jets by Kuensch et al. (2014), and a 0.8 power law of the axial penetration length was fitted to the data. In this study, two-stage power laws are observed before and after the collapse of the hollow cone. The slight depression in the axial penetration plot shows the collapsing events consistent with the previous observations. A 0.65 power law is observed during the initial development phases when the hollow cone remains intact, whereas later a 0.8 power law fits well. For the maximum width, a range of values is obtained as discussed before. The range widens as the jet develops and can be as large as 15 mm away from the nozzle. While Kuensch et al. (2014) found a 0.2 power law of the maximum width, in this study, two-stage power laws are

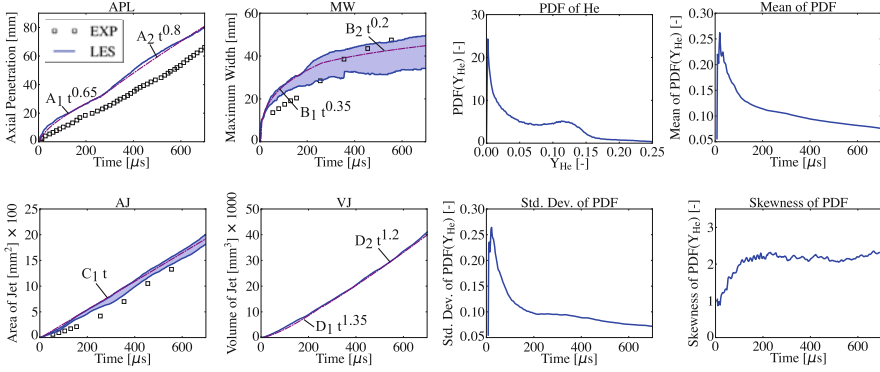


**Fig. 4.17** Comparison of characterizing parameters between experiment and LES

observed with an initial 0.35 power law behavior and 0.2 power law after the collapsing event. The area of the jet increases linearly with time, which is also consistent with the product of power laws of the axial penetration length and the maximum width. In summary, this leads to

$$AJ \sim APL_{1,2} \cdot MW_{1,2} = C_1 t \quad (4.1)$$

$$VJ_1 \sim APL_1 \cdot MW_1 \cdot MW_1 = D_1 t^{1.35} \quad (4.2)$$

$$VJ_2 \sim APL_2 \cdot MW_2 \cdot MW_2 = D_2 t^{1.2} \quad (4.3)$$

The subscripts, 1 and 2, denote the first and the second stage of the jet evolution, respectively. The jet volume increases continuously as the jet entrains ambient gas into the jet volume. The product of the power laws of the maximum width and the axial penetration (Eqs. 4.2 and 4.3) follow the LES predictions quite well. These scaling laws can be used for getting the first estimates of the probable gas jet behavior. However, the constants of proportionality must be known beforehand. The mass-weighted PDF of the helium mass fraction at  $t = 700 \mu\text{s}$  is also shown in Fig. 4.17. The probability of finding no helium anywhere in the jet volume is zero because the jet volume is obtained with the chosen threshold of 0.001 for helium mass fraction ( $Y_{\text{He}}$ ). A bimodal PDF can be observed. The statistics of the PDF, mean, standard deviation, and skewness provide information on the quality of the mixture. These are plotted for the duration of the simulation. The mean values are the indicators of the average helium mass fraction within the jet volume. The mean of the PDF increases to a peak value very quickly after the start of injection (SOI) indicating a very rich mixture. As more and more ambient air is entrained and mixed with helium, the mean value decreases nonlinearly. The standard deviation quantifies the degree of mixing. Higher standard deviation indicates less homogeneous mixture and vice versa. The standard deviation of the PDF shows a similar trend to that of the mean and is of the same order, implying a high degree of

inhomogeneities in the mixture. The third standardized moment of the PDF, skewness, is the indicator of pockets of lean or rich mixture. Positive values show the presence of pockets of rich mixture, while negative values show the presence of lean regions in the jet volume. Here, the skewness of the PDF is very high initially and positive, which drops quickly and again increases gradually. Initial large positive values are expected because the mixing of helium has not started yet. With the progress of mixing, the skewness drops. The gradual increase of the skewness indicates the increasing presence of unmixed rich regions of helium.

Overall, the macroscopic characteristics such as the axial penetration, the maximum width, and the collapsing event of the hollow cone can be reasonably predicted by the LES with the used mesh resolution. The LES was run on 1024 cores for 131 h, which is quite expensive for such a short duration of injection. Therefore, the potential reasons for the discrepancies between experiment and simulation are investigated using a computationally less expensive URANS approach. However, URANS requires modeling of energy-containing turbulent scales, and several turbulence models have been developed for different applications. Some of them have become a standard in industrial simulations, e.g., RNG  $k-\varepsilon$ , realizable  $k-\varepsilon$ , and SST  $k-\omega$ . Before applying these in the simulations of the gas injection, these turbulence models are evaluated in terms of macroscopic characteristics against the LES, which relies on the Vreman model for the sub-filter eddy viscosity.

#### 4.2.6 Choice of Turbulence Model

The RNG  $k-\varepsilon$  model has been developed from the Navier–Stokes equations through the renormalization group (RNG) theory (Yakhot and Orszag 1986). The renormalization group method is based on statistical averaging of fluctuations on all scales, ranging from the smallest scale to successively larger scales, which is particularly appropriate for the description of turbulence involving a wide range of scales (Wilson 1983). Therefore, the effects of different length scales on turbulent diffusion are intrinsically modeled by the RNG  $k-\varepsilon$  model. Also, the model constants are deduced analytically. The realizable  $k-\varepsilon$  model ensures physically realistic values of the turbulent kinetic energy by constraining the positivity of normal Reynolds stresses and obeying the Schwarz’s inequality for turbulent shear stresses (Shih et al. 1995). The realizable  $k-\varepsilon$  model performs well for rotational flows. The shear stress transport (SST)  $k-\omega$  model by Menter (1994) is the combination of the standard  $k-\varepsilon$  model and the standard  $k-\omega$  model, which has the benefits of both models. The standard  $k-\omega$  model is advantageous for boundary layer flows and modeling of the near-wall viscous regions. A blending function is used, which is zero close to walls, activating the  $k-\omega$  model, and unity away from walls, leading to the  $k-\varepsilon$  model. The effects of high-pressure gradients are also considered for calculating the eddy viscosity. The SST  $k-\omega$  model is well suited for external flows, such as in aerodynamic applications. Nevertheless, it is investigated in this study

because high-pressure gradients and flow separation occur near the exit of the nozzle.

The initial and boundary conditions for the URANS simulations are maintained as in the LES for a direct comparison. The temporal jet evolution is investigated with the turbulence models. A quantitative analysis of the performance of URANS models is made and compared with the LES (see Fig. 4.18). The experimental values are plotted for reference. Compared to the LES, all turbulence models used here predict the initial axial penetration length reasonably, although the collapsing instant as indicated by the depression in the plots is slightly delayed. The maximum width is predicted well; however, the range of values is smaller at later times. More substantial differences between the turbulence models can be observed in the area of the jet and are more prominent in the volume of the jet. Comparing the volume of the jet, the RNG  $k-\varepsilon$  model is the closest to the LES, which is very important for mixing as the amount of entrained ambient air affects the mixture quality. This is reflected in the mean of the PDF of  $Y_{He}$ , which is lower for all turbulence models compared to the LES due to a higher amount of air entrainment. Again, the RNG  $k-\varepsilon$  model comes closer to the LES. The standard deviation shows a distinct bump in the URANS results, which is the effect of the hollow-cone collapse. The skewness of the PDFs shows a similar trend in the URANS compared to the LES. However, the development of the trend is delayed, and the absolute values are high with all turbulence models, which implies a high probability of finding rich helium regions in the jet volume. It can be distinctly observed that the mixing statistics, in general, can be entirely different although other global characteristics are very similar. Based on the overall performance with respect to macroscopic characteristics on the typical mesh resolutions used in the full engine simulations, the RNG  $k-\varepsilon$  model can be a good choice compared to the other two models considered here and is chosen for further URANS simulations in this study.

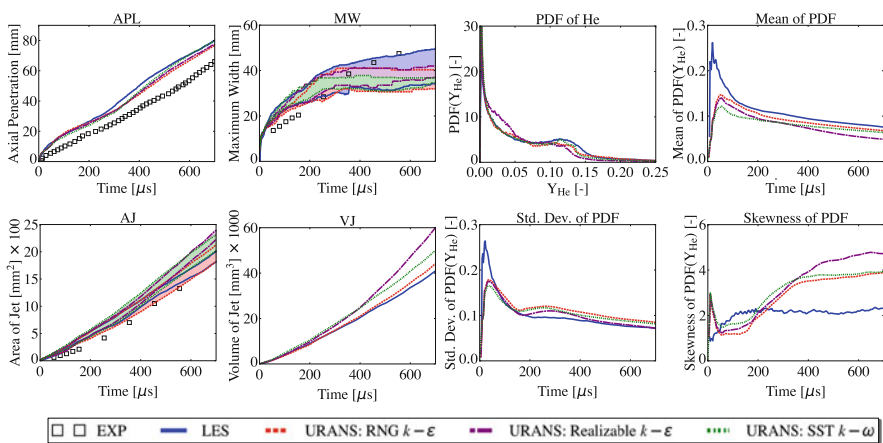


**Fig. 4.18** Comparison of characterizing parameters obtained with different URANS turbulence models and LES



### 4.2.7 Needle Motion and Initial Conditions

The initial nonlinear behavior of the temporal gas jet development observed in the LES caused an overprediction of the axial penetration. In the LES, the needle lift is fixed resulting in a higher mass flow rate from the beginning. In practice, the needle does not open instantly. There is always a delay in opening; depending on the type of injector used, the opening can be very fast as in piezoelectric injectors, or it can be relatively slow as in solenoid injectors. Since the injector in this study is of the solenoid type, the opening profile is expected to be gradual. The needle lift profile is shown in Fig. 4.19a, where the opening delay is  $\sim 100 \mu\text{s}$ . Initially, the needle is in a closed position, and the domain is divided into two regions: a high-pressure upstream region with helium at a pressure of 15 bar and a temperature of 298 K and a low-pressure downstream region. A second initial condition (IC2) for the fixed needle case (keeping the same needle lift) is also considered in this study because it is more similar to the initial conditions in the injector with a closed needle. The domain is divided into two regions at the valve seat location as shown in Fig. 4.19b. The IC2 mimics the sudden opening of the needle.

URANS simulations with the needle lift profile are carried out, and as expected, the linear behavior in the initial stages of the gas jet development is reproduced well by the simulation with needle motion (see Fig. 4.20). However, the plot diverges from the experimental values after  $400 \mu\text{s}$ , probably due to the collapse of the hollow cone. To investigate the deviation, the pressure below the poppet is monitored and plotted in Fig. 4.21. The collapsing event in the simulation with needle lift is delayed significantly, causing more than 50% decrease in the axial penetration length compared to the fixed needle simulations with IC1. In contrast to this study, Kuensch et al. (2014) reported a nonlinear behavior of the axial penetration in the experiments with the hollow-cone injector. However, a piezoelectric injector was used in their investigations, which is very fast compared to the solenoid-actuated Delphi injector. Therefore, for piezoelectric injectors, it may be concluded that the

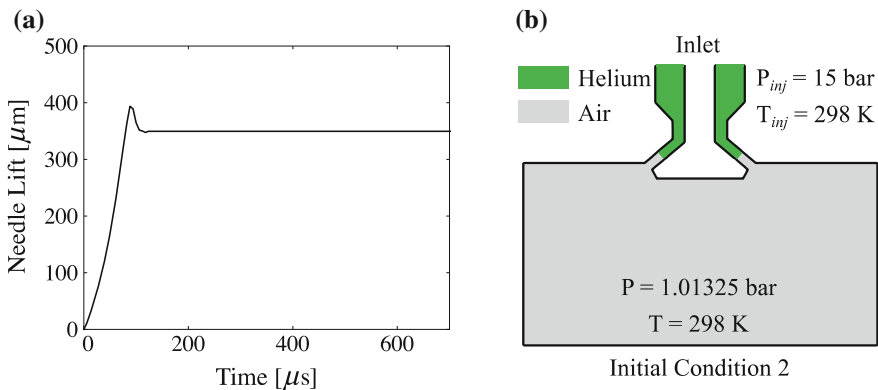


**Fig. 4.19** Needle lift profile (a) and initial condition 2 (b) in the nozzle

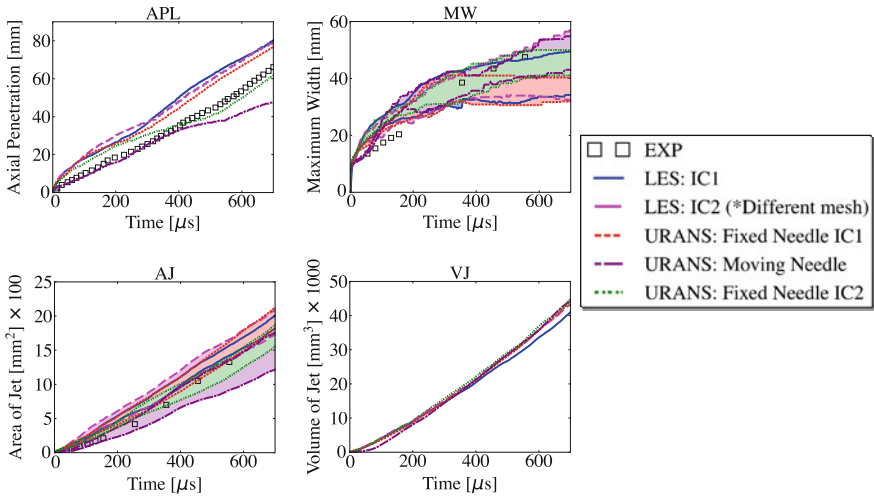


Fig. 4.20 Effect of initial conditions and the needle motion on the characterizing parameters

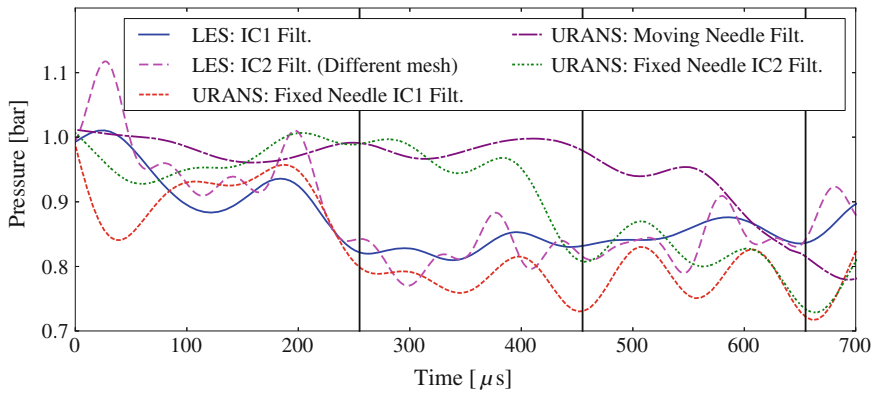


Fig. 4.21 Pressure monitor below the poppet: vertical black lines  $t = 255 \mu\text{s}$ ,  $t = 455 \mu\text{s}$ ,  $t = 655 \mu\text{s}$  indicate the event of hollow-cone collapse for respective cases

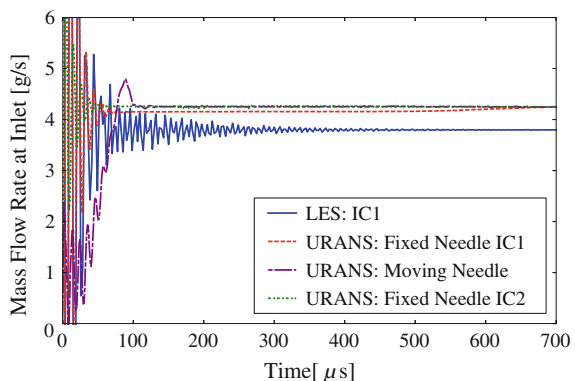
needle motion may not be important for prediction of the initial phase of the gas jet development. The second initial condition, IC2, was tested using URANS and LES with a mesh resolution lower than used before. The URANS simulations with IC2 predict the initial nonlinear behavior similar to that observed with IC1. However, as the hollow-cone collapse is delayed (see Fig. 4.21), the axial penetration drops. After the collapse, the single coherent gas jet follows a linear increase in the axial direction. The maximum width and the area of the jet closely follow the experimentally measured values for the case with needle motion and fixed needle with IC2. For the moving needle case, the volume of the jet increases slowly but later

converges to the other URANS cases, indicating similar air entrainment for all URANS cases. To verify the effect of initial conditions on the collapsing behavior of the jet, an LES with IC2 is performed. However, a lower mesh resolution was used in this case to keep the computational costs lower. In contrast to the corresponding URANS case, the LES with IC2 shows a very similar axial penetration to that with IC1, and the collapsing event is only slightly delayed.

The needle motion and initial conditions influence the mass flow rate through the nozzle during the initial phases. The mass flow rate at the inlet of the nozzle for different cases is shown in Fig. 4.22. The shock/pressure waves propagating inside the nozzle and their reflections from the complex internal geometry cause the initial fluctuations. The waves survive for long times in the LES due to low-dissipation numerical schemes and dissipate quickly in the URANS simulations. The viscous boundary layer flow is resolved better in the LES using a high-resolution stretched grid near the walls, whereas the near-wall velocities are modeled with log law in the URANS simulations with a coarse cut-cell Cartesian grid. Therefore, the values of the mass flow rate in the LES are lower than those in the URANS simulations. Initially, the mass flow rate in the URANS simulation with initial condition IC1 is marginally lower but later merges with the mass flow rates for the cases with needle motion and initial condition IC2.

The consideration of the needle motion is crucial for accurate resolved simulations of the poppet-type gas injectors, particularly for solenoid-actuated injectors. For piezoelectrically actuated poppet-type injectors, the fixed needle approach may be sufficient. The initial conditions in the nozzle are important for the further development of the gas jet. With the chosen mesh resolution and turbulence model, the URANS simulations showed sensitivity to different initial conditions, whereas the LES did not predict such distinction. The URANS computations required 8–25 h on 24 cores, which is less by, at least, a factor of 200 compared to the LES. Further investigations using high-fidelity LES with a moving needle are necessary to identify the reasons for the discrepancies with respect to the experiments. Moreover, the sensitivities of the URANS approach to the initial conditions in the nozzle need to be examined.

**Fig. 4.22** Mass flow rate at the inlet in LES and URANS with different initial conditions and the needle motion



## 4.3 Modeling of Poppet-Type Gas Injectors

### 4.3.1 *Challenges in Numerical Simulations*

Resolved simulations of the poppet-type gas injectors have already been described as challenging and computationally very expensive mainly because of different length and timescales present inside the injector and the cylinder. Therefore, it is important to reduce the simulation run-time to be able to use numerical simulations in the engine design process that motivates the splitting of the full simulation considering it as a multi-scale problem and development of simplified models for the process with smaller timescales. There have been a few attempts in the literature for the development of such models. A computational model was developed for a cylindrical orifice by Johnson et al. (1995) for hydrogen gas injection and combustion. The model was based on the inflow conditions calculated from choked nozzle flow dynamics. The model replaced the nozzle flow dynamics and reduced the run-time of the full simulation by a factor of 10. Another model for high-speed jets was developed by Mather and Reitz (2000), which was based on compressible under-expanded nozzle flow with a barrel shock and a Mach disk. Sonic flow was assumed at the Mach disk, and the diameter of the Mach disk (called equivalent diameter) was calculated from the nozzle exit pressure and ambient gas pressure. The jet exit velocity and density were obtained from an isentropic expansion process and used as the inflow boundary condition. The jet penetration was found to be dependent on the momentum injection rate by Ouellette and Hill (1999). They proposed to simply impose momentum as a boundary condition at the nozzle exit. Most models were developed for cylindrical orifices, while the modeling efforts for the poppet-type outwardly opening design have been relatively scarce due to the more complex geometry. Some of the models are described in the following sections.

### 4.3.2 *Converging–Diverging Nozzle Approximation*

Considering the similarity between high-speed round jets and the resulting single gas jet from a shrouded poppet-type valve, Kim et al. (2007) proposed to use a simplified converging–diverging nozzle design. The throat area of the simplified nozzle and modified injection pressure were obtained using quasi-one-dimensional isentropic flow relations from the downstream characteristic Mach number and fuel mass flow rate corresponding to the original valve. However, this model is limited to shrouded poppet-type nozzles.

### 4.3.3 Source Modeling Approach

A virtual injector model for a poppet-type valve based on the source terms in the governing equations was developed by Baratta et al. (2011). In this model, the injector needle is opened to the maximum lift and the geometry upstream of the throat section is removed from the computational domain. The mesh cells at the throat section are treated as the injection source cells. The source terms in the governing equations are computed as  $S_\phi = \dot{m}\Phi$ , where  $\dot{m}$  is the mass flow rate through the injector and  $\Phi$  is the flux in each of the equations. This approach is valid for supersonic injection velocities as downstream conditions do not affect upstream flow properties in supersonic flows. However, the approach does not include the effects of upstream nozzle geometry, which are typically important.

### 4.3.4 Mapped Boundary Condition Approach

The mapped boundary condition (MBC) approach was recently proposed by Deshmukh et al. (2016), where the simulation is split into two parts: nozzle flow and in-cylinder flow. This approach retained the geometrical information of the nozzle and provided accurate boundary conditions for the in-cylinder flow simulation. In this approach, a stand-alone nozzle simulation, either LES or URANS, is carried out for a desired pressure ratio. The nozzle flow and near-nozzle flow reach a steady state within a short time compared to the duration of injection. The injector nozzle is decoupled from the cylinder by slicing it from the computational domain along an arbitrary surface, which is treated as the mapping boundary on the cylinder. Since the flow at the nozzle exit is supersonic due to high-pressure ratio, the downstream flow conditions have no effect on the upstream flow field. On the other hand, under subsonic conditions, the upstream flow field depends on downstream flow conditions, and hence, the one-way mapping is not accurate. Therefore, the MBC approach is physically more accurate under supersonic nozzle flow conditions. The flow variables in the nozzle simulation are recorded at the mapping boundary and then transferred onto the corresponding inflow boundary of the full-scale simulation. The approach is illustrated in Fig. 4.23.

The location of the mapping boundary is selected based on two opposing criteria:

1. The mapping boundary should be far off from the nozzle exit so that the velocity is small enough to increase the time step significantly.
2. The mapping boundary should be close to the nozzle exit to avoid removal of a large volume from the computational domain.

An ideal mapping location is at the end of the Mach disk, which is consistent with the models reported in the literature (Johnson et al. 1995; Mather and Reitz 2000; Ouellette and Hill 1999). However, in this study, the mapping boundary is

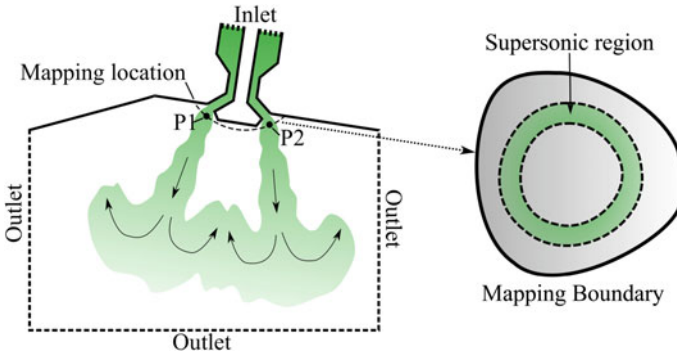


**Fig. 4.23** Sketch illustrating the mapped boundary condition approach

located at 1 mm downstream of the nozzle to avoid cutting into the cylinder volume. This location is found to be sufficient to obtain large time steps and reasonably accurate predictions of the in-cylinder flow fields. Nevertheless, further work is necessary to determine the optimum location for the mapping boundary.

To generate the mapped boundary condition, a stand-alone nozzle flow simulation is performed. The injector needle is opened to its maximum lift and the domain is initialized into two regions with an initial discontinuity at the valve seat. The upstream region containing helium is set to the specified injection pressure and temperature, and the downstream region is initialized with a low pressure corresponding to ambient conditions. A total pressure boundary condition is set at the inlet, and a non-reflecting characteristic boundary condition is applied at the outlet. Remaining boundaries are treated as no-slip, adiabatic walls. The simulation is run and continued until statistically stationary conditions are reached at the mapping location. It can be verified whether the near-nozzle flow has reached a statistically stationary condition. For example, Fig. 4.24 shows the plot of velocity magnitude at two locations, P1 and P2, on the mapping surface over time for pressure ratios of 15 and 8. The instantaneous signal is fluctuating; therefore, it is filtered to get the mean velocity magnitude. The mean velocity magnitude becomes steady after  $\sim 60 \mu\text{s}$ . The interaction of shock waves and the geometrical features of the cylinder head are also captured.

The flow field variables downstream of the nozzle exit for two pressure ratios are shown in Fig. 4.25 in the  $Y = 0.0$  plane at time  $t = 75 \mu\text{s}$ . A dashed line indicates the mapping location. The flow variables such as velocity, density, temperature, and mass fractions at the mapping location are recorded and stored. The flow variables are mapped only in the supersonic regions, which is geometrically marked based on the mass fraction of injected gas. Here, it is observed that the entrainment of ambient gas in the supersonic gas jet at the mapping location is negligible. The threshold helium mass fraction to mark the supersonic region is chosen based on a trade-off between the thickness of the supersonic region and mesh resolution. For example, it is set to 0.7 for the pressure ratio of 15 and 0.6 for the pressure ratio of

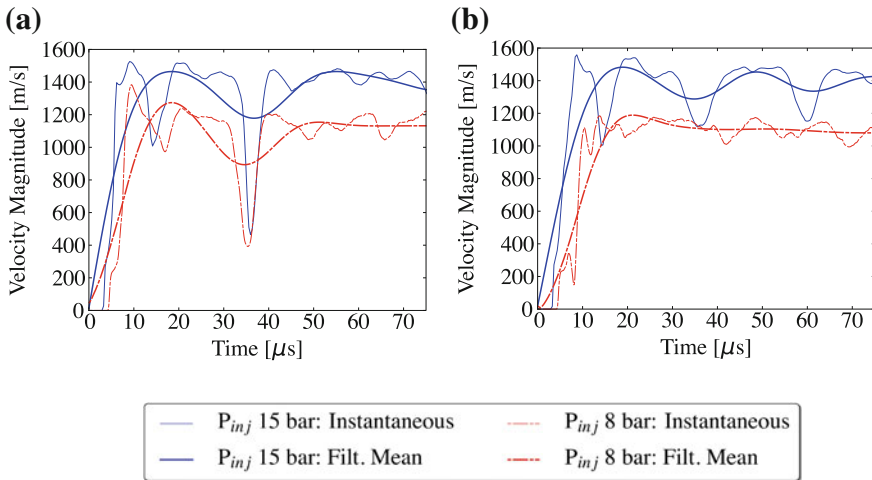


**Fig. 4.24** Velocity magnitude monitored at location P1 (a) and P2 (b) on the mapping surface

8. After the mean flow quantities reach a statistically stationary state, they are averaged in time. The resulting inflow profiles of different flow variables on the inflow boundary are also shown in Fig. 4.25. The remaining area outside the supersonic region should mimic a wall boundary and is set to zero velocity and a fixed temperature avoiding additional inflow through this area. A zero-gradient condition for pressure is required over the mapping boundary to get constant mass flow across it. The effects of needle motion are important for solenoid-actuated injectors as shown before, especially at high engine speeds. These can be considered by gradually ramping up the velocity components at the mapping boundary. At relatively lower engine speeds (e.g., 1000–2000 RPM in this study), the needle opening period in terms of crank angles is small enough and does not largely affect subsequent mixture formation. Moreover, the conditions at the mapping location do not change significantly during the injection period at lower engine speeds. Therefore, the inflow profiles are fixed in time.

For a supersonic inflow boundary, all characteristic waves enter the flow domain; therefore, all information should come from outside of the domain (Hirsch 1994). For a system of compressible Navier–Stokes equations with a non-reacting scalar, at least six flow variables, namely density, three components of velocity, temperature, the mass fraction of helium, are required. Neglecting the contribution of sub-filter scales, these are sufficient for an LES. However, for a URANS simulation, two additional equations for the turbulence model need turbulent kinetic energy (TKE) and turbulent dissipation rate to be specified at the inflow boundary. Depending on the method used for the stand-alone nozzle flow simulation, some variables are directly available, and the rest need to be estimated from the available ones and specified as a constant value in the supersonic region. For example, a mapping from a stand-alone nozzle flow LES to an LES of full-scale simulation (LES-to-LES mapping) or URANS-to-URANS mapping will not require any

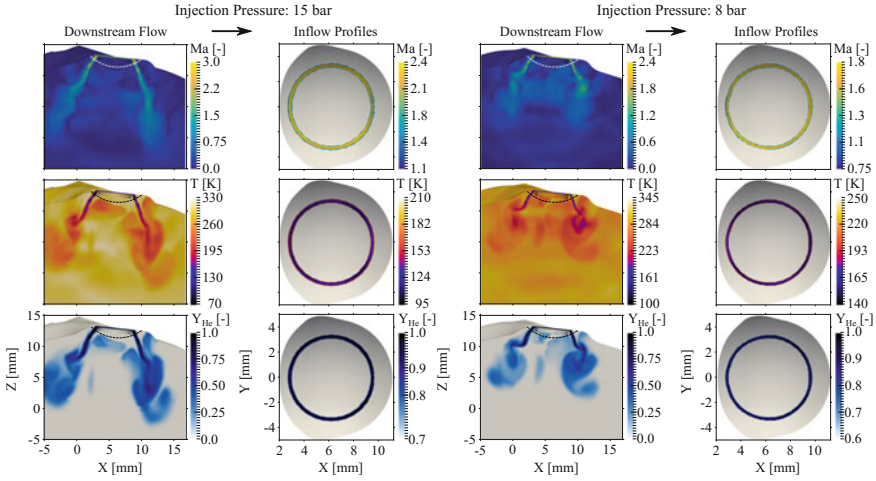


**Fig. 4.25** Downstream spatial distribution of Mach number (Ma), temperature ( $T$ ) and helium mass fraction ( $Y_{He}$ ) in  $Y = 0.0$  clip plane and resulting inflow profiles at time  $t = 75 \mu s$  in nozzle simulations for injection pressures 15 bar (*left*) and 8 bar (*right*)

estimation, whereas for the LES-to-URANS mapping the TKE is estimated from the fluctuating velocity components obtained from the time-averaged mean velocity profile from the LES. The turbulent dissipation rate is calculated using Eq. 4.4 from the TKE and an appropriate length scale ( $le$ ), which is chosen as a fraction of the maximum valve lift.

$$\epsilon = \frac{c_{\mu}^{3/4} k^{3/2}}{le} \tag{4.4}$$

where  $c_{\mu}$  ( $=0.09$ ) is a model constant. The TKE could also be specified in terms of estimated turbulent intensity and an appropriate dissipation length scale. However, the sensitivity of the results to the estimated kinetic energy and dissipation rates needs further investigation in the future.

## 4.4 Application of Mapped Boundary Condition Approach

### 4.4.1 Case Description

The MBC approach is demonstrated in a quasi-steady-state flow configuration and a full-cycle engine configuration. For validation, the in-cylinder velocity field is measured for an optically accessible single-cylinder research engine. All of the experimental data has been measured at the Institute of Aerodynamics (AIA) of RWTH Aachen University. The injector was provided by Delphi, and helium was



**Table 4.1** Engine specifications

Displaced volume	364 cc
Bore	75 mm
Stroke	82.5 mm
Connecting rod	146 mm
Compression ratio	7.4
Number of valves	4
Valve lift	9 mm
Exhaust valve open	250° BTDC
Exhaust valve close	33° ATDC
Inlet valve open	34° BTDC
Inlet valve close	250° ATDC

used for injection. The physical properties of helium are different from natural gas. Based on isentropic flow calculations, helium results in 46% lower mass flow and 13% higher momentum flow compared to natural gas through the injector at a given pressure ratio. Nevertheless, this study can reasonably provide an insight into the underlying processes occurring due to gas injection and their impact on the in-cylinder flow field and mixture formation. Table 4.1 shows the engine specifications. The valve opening and closing events are with reference to the non-firing TDC, which is set to 0° crank angle.

The velocity field has been measured using state-of-the-art time-resolved stereoscopic particle image velocimetry (PIV) (see the experimental setup in Fig. 4.26a). The measurement cases chosen for comparison with the simulations are shown in Table 4.2. The poppet-type injector is positioned between the two intake valves inclined at an angle of 6° with an offset of 6 mm from the axis of the cylinder. The maximum needle lift of the injector is 350  $\mu\text{m}$  in all measurement cases. For the steady-state measurement of the velocity field, helium at a pressure of 15 bar is injected for one second in a fully closed cylinder with the piston at the bottom dead center (BDC). Initially, the cylinder is at atmospheric pressure and temperature. The velocity field is measured in two planes passing through the injector and perpendicular to each other as shown in Fig. 4.26b. During the injection, 500 samples of the velocity field are recorded, beginning at 100 ms after SOI until 167 ms at a frequency of 750 Hz. The sampling starts 100 ms after SOI to obtain a fully developed mixture of the injected and the in-cylinder gas. For the full engine cases (transient 1–3), the measurements are carried out on two planes except for case transient 3, where the velocity field is measured only in the  $Y = 0.0$  plane. Three hundred and twenty-one consecutive cycles are recorded during the measurements to obtain a high convergence of the data. In one cycle, 17 images are recorded with an interval of 16° crank angle with a sampling frequency of 375 Hz for the engine speed of 1000 RPM and 750 Hz for the engine speed of 2000 RPM. Measurements are performed only during the intake and compression phase, beginning at a crank angle of 72° ATDC until 328° ATDC.

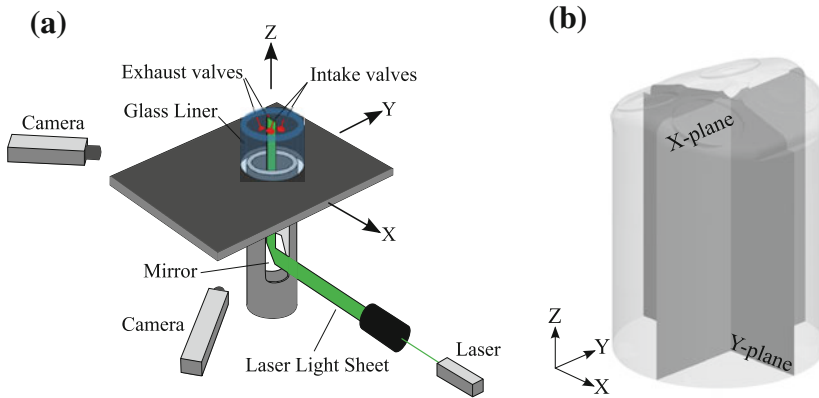


**Fig. 4.26** Experimental setup (a) and measurement planes (b) for time-resolved stereoscopic PIV

**Table 4.2** PIV measurement cases

Case	Engine speed (RPM)	$P_{inj}$ (bar)	SOI (ms)	DOI (ms)	SOI (CA°)	DOI (CA°)
Steady	0	15	0	1000	–	–
Transient 1	2000	15	–	6	90	72
Transient 2	1000	15	–	6	90	36
Transient 3	2000	8	–	3	135	36

#### 4.4.2 Steady-State Configuration

The measurements of the velocity field begin 100 ms after SOI, and as shown in Fig. 4.27, the pressure in the cylinder rises continuously from 1 to 5.5 bar up to the start of measurement as the valves are closed. Therefore, the simulation, if begun from the start of injection, would have to be run for more than 100 ms to capture this pressure rise, which is impractical from a numerical point of view. The initial estimate of the time required for running one such LES without any modeling of nozzle flow was in the order of months on the available computing resources, which is unrealistic. A more practical approach is considered here. Because of the inherent transient nature of the physical process, it cannot reach a steady state. Therefore, a timescale is defined based on the physical dimensions of the domain and the speed of sound in the fluid, here air, in the domain. The timescale is used to roughly estimate the time required for the velocity field to reach a *quasi*-steady state. In this case, the maximum dimension is along the axis of the cylinder ( $\sim 0.1$  m). Speed of sound in air is  $\sim 343$  m/s. So, the time required for a pressure wave to reach the bottom of the cylinder is approximately 0.3 ms. It is assumed that a *quasi*-steady state is reached when the pressure waves have traveled across the cylinder multiple times so that they no longer change the flow field significantly. Hence, the actual simulation time to reach the *quasi*-steady state is assumed to be in multiples of the

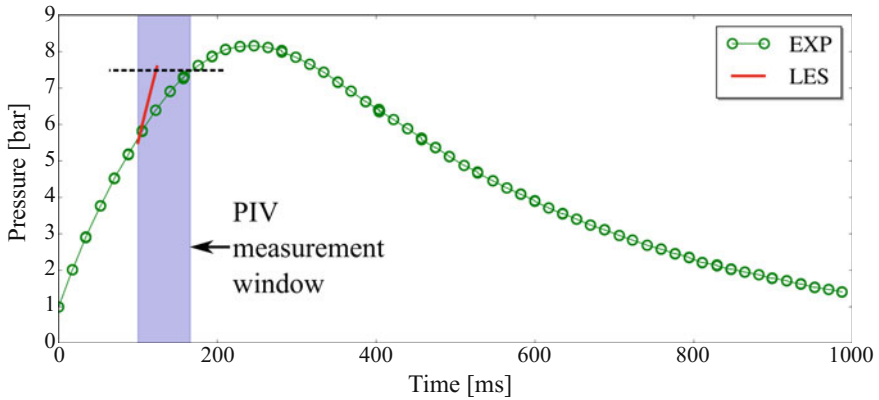


**Fig. 4.27** Chamber pressure measured during PIV with  $P_{inj}$  15 bar

characteristic time  $T$  ( $\approx 0.3$  ms), and  $70 * T \sim 21$  ms was found to be sufficient in this study. The simulation is directly started 100 ms after the SOI with the initial cylinder pressure of  $\sim 5.5$  bar. Within the measurement window, the pressure rises up to  $\sim 7.5$  bar. Both LES and URANS simulations were carried out and compared with velocity field measurements. The LES shows the pressure rise of  $\sim 2$  bar in the time required to reach the *quasi*-steady-state (21 ms) compared to 67 ms required for the same pressure rise in the experiment. This is because blow-by losses were not considered in the simulations. An unstructured mesh was used with the high-fidelity compressible LES solver (CHRIS), and a Cartesian cut-cell mesh was used in CONVERGE for the URANS, which are not shown here for brevity. With this simulation approach, it was possible to reduce the simulation run-time significantly, from the order of months to the order of days.

The instantaneous and time-averaged velocity magnitude in the  $X$ - and  $Y$ -plane is shown in Fig. 4.28. The gas jet penetrates the cylinder, hits the bottom, and reverses resulting in a recirculation zone moving it sideways in the  $X$ -plane. As said before, the simulation required 70 characteristic times, i.e., 21 ms, to reach a *quasi*-steady-state. This can be verified by monitoring the velocity components at different points in the cylinder. For example, four points are monitored in the  $Y$ -plane, and the velocity components at these points are plotted in Fig. 4.29. The instantaneous signals are filtered to get mean values to identify trends. It can be observed that the mean signal does not change significantly after 21 ms. The simulation is continued until 80 characteristic time units, i.e., 24 ms, and a window of 3 ms is used for time-averaging.

A direct comparison of instantaneous  $W$ -velocity from the LES and PIV in the  $X$ -plane is shown in Fig. 4.30. Qualitatively, the LES predicts the gas jet location and sideways motion. After analyzing the experimental data, it was found that the jet is not visible in all of the measured samples because it fluctuates vigorously and moves out of the measurement plane. In fact, only selected samples show the gas

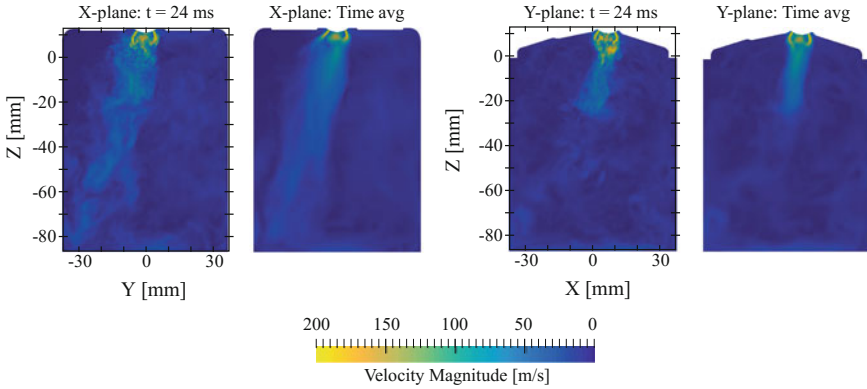


**Fig. 4.28** Velocity magnitude in LES on two planes; instantaneous field at  $t = 24$  ms and time-averaged field ( $t = 21$ – $24$  ms)

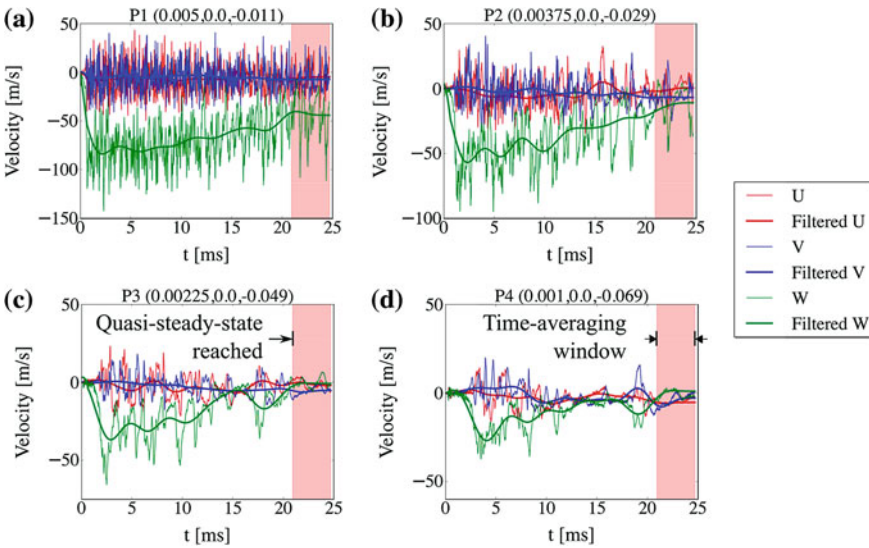


**Fig. 4.29** Velocity components monitored at four locations in the  $Y$ -plane

jet, indicating a large variability in the measurements. This is important when averaging the experimental data.

On the other hand, the time-averaged velocity field from the LES can be directly compared with that from the URANS simulation (see Fig. 4.31) because URANS ideally should provide ensemble-averaged results. The URANS predicts velocity magnitudes qualitatively similar to the LES. The strong sideways movement of the gas jet is not predicted in the URANS simulation, although the flow field is asymmetric. URANS cannot be expected to capture the dynamic large-scale

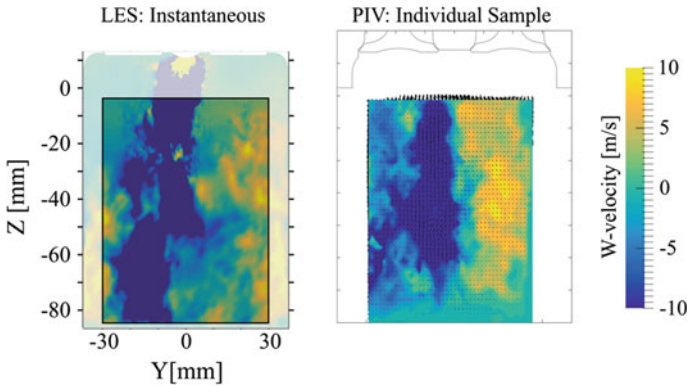


**Fig. 4.30** Comparison of LES (*left*) and PIV experiment (*right*) in the X-plane (*instantaneous fields*)

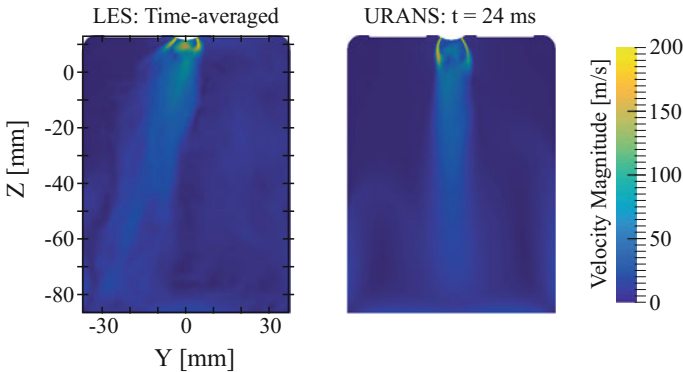


**Fig. 4.31** Comparison of time-averaged ( $t = 21\text{--}24$  ms) velocity magnitude in the LES (*left*) and the instantaneous one at  $t = 24$  ms in the URANS simulation (*right*) in the X-plane

motions of the gas jet due to the inherent modeling of energy-containing turbulent length scales.

For a more quantitative comparison, the velocity magnitude from the simulations and the experiments is plotted at certain locations in the cylinder (see Fig. 4.32) in the X-plane and the Y-plane. The gray curves in the background indicate instantaneous velocity magnitudes in LES, while gray symbols indicate the individual experimental snapshots only where the gas jet is present in the plane. Red curves show time-averaged LES, blue curves show URANS results, and green symbols are ensemble averages of individual experiments. The LES can reasonably capture the ensemble-averaged velocity field as well as the instantaneous fluctuations. On the other hand, URANS predicts the magnitudes of the ensemble-averaged velocity field, although the peak locations are not predicted. This is again because of the

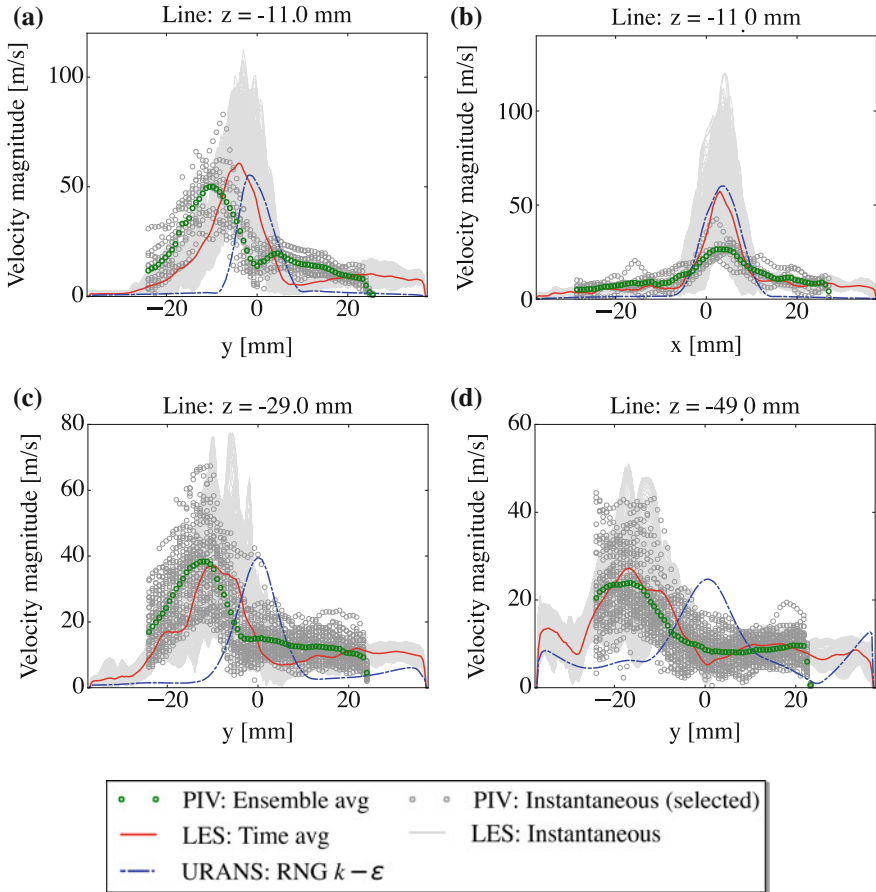


**Fig. 4.32** Comparison of LES and URANS with PIV experiments at different locations

intrinsic limitations of the URANS turbulence modeling. In the  $Y$ -plane, the gas jet is not fully visible due to sideways movement in the  $X$ -plane. Therefore, only one location is plotted in Fig. 4.32b.

### 4.4.3 Full Engine Configuration

**Simulation Setup.** The simulation setup for the engine simulation is shown in Fig. 4.33a. The domain is split into three regions: cylinder, exhaust, and intake. The injector is sliced out from the computational domain for the MBC approach. CONVERGE generates a Cartesian cut-cell mesh at run-time. The base mesh size of 4 mm is used, and embedded refinement regions are placed in the cylinder, which results in a mesh size of 1 mm. The AMR is activated to capture gradients in

velocity and scalar fields. The mesh is refined at certain boundaries and/or regions to capture the physical fields and their gradients accurately. A representative mesh in the simulation during the intake stroke is shown in Fig. 4.33b.

Initially, a simulation of a full engine cycle is performed without injection for two engine speeds, 1000 and 2000 RPM, with air as a working fluid. To avoid the effects of initial quiescent conditions, the simulation is run for four cycles to set up a tumble flow field inside the cylinder. For the simulations with injections, the computational domain is initialized with the flow field just before the SOI.

A total pressure boundary condition is applied at the hemispherical inlet with a pressure of 101.325 kPa and a temperature of 298 K. A time-varying pressure boundary condition based on measured data is imposed at the outlet of the exhaust pipe. Gradients of velocity and temperature at the exhaust pipe are set to zero. Other boundaries are modeled as no-slip walls with a fixed temperature of 298 K. For further details on the simulation setup, initial and boundary conditions, the reader is referred to Deshmukh et al. (2018c).

The MBC approach is used in place of the injector. The MBCs are generated for two injection pressures, 15 and 8 bar, using the LES solver. As the URANS solver of CONVERGE is used for the engine simulations, this is an LES-to-URANS mapping for MBC. Therefore, the TKE and turbulent dissipation rates are required to be estimated from the LES data at the mapping location. The time-averaging is performed on the inflow profiles to obtain the TKE. The turbulent dissipation rate is computed using Eq. 4.4. The length scale ( $l_e$ ) is chosen as  $\sim 15\%$  of the maximum valve lift resulting in the values reported in Table 4.3 for two injection pressures.

The injection mass flow rates across the mapped boundary for injection pressures of 15 and 8 bar are shown in Table 4.4. For comparison, the injector mass flow rates measured in separate constant volume chamber experiments at the injection pressures of 16 and 11.8 bar are provided. Additionally, the mass flow rates from isentropic flow calculations are given for reference. In general, the isentropic calculations predict higher mass flow rates compared to the measured values and those from the LES, except for the injection pressure of 8 bar.

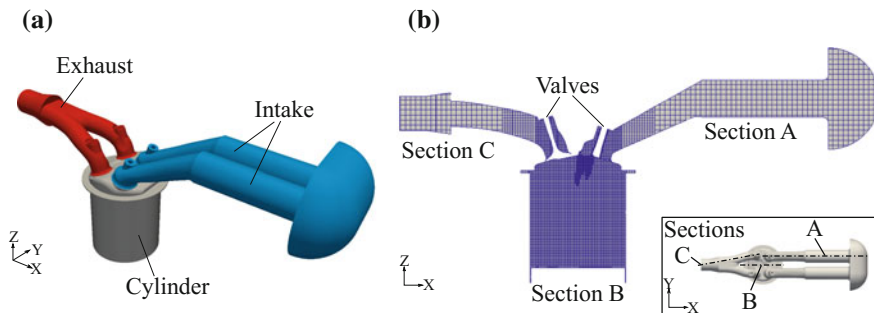


**Fig. 4.33** Computational domain (a) and representative mesh (b)

**Table 4.3** TKE and turbulent dissipation rate estimated for two injection pressures

Injection pressure (bar)	TKE (m <sup>2</sup> /s <sup>2</sup> )	Turbulent dissipation rate (m <sup>2</sup> /s <sup>3</sup> )
15	6.001 × 10 <sup>4</sup>	4.423 × 10 <sup>10</sup>
8	2.979 × 10 <sup>4</sup>	2.194 × 10 <sup>10</sup>

**Table 4.4** Measured and calculated mass flow rates through the injector for different injection pressures

Injection pressure (bar)	Measured (g/s)	LES (g/s)	Isentropic calculations (g/s)
16.07	3.5	–	4.45
15	–	3.8	4.15
11.79	2.5	–	3.26
8	–	2.3	2.21

For validation of the MBC approach for full-cycle engine simulations, a direct comparison can be made between PIV measurements and simulations in terms of velocity magnitude. Alternatively, derived quantities of interest, such as the tumble number, can be compared. The tumble number is a quantitative measure of the in-cylinder charge motion about the instantaneous volumetric center of the cylinder relative to the engine speed. The following expression is used for the calculation of a planar tumble number from both PIV data and simulations:

$$\text{Tumble Number} = \frac{\sum_{i=0}^n [(Z_i - Z_{ca})U_i - (X_i - X_{ca})W_i]}{\omega_{\text{crank}} \sum_{i=0}^n [(Z_i - Z_{ca})^2 + (X_i - X_{ca})^2]} \quad (4.5)$$

where

$\omega_{\text{crank}} = \frac{2\pi N}{60}$  (Hz), angular speed of the crankshaft

$N$  = engine speed (RPM)

$U_i, W_i$  = X- and Z-components for velocity at point  $i$  (m/s)

$X_i, Z_i$  = X- and Z-coordinates of point  $i$  (m)

$X_{ca}, Z_{ca}$  = X- and Z-coordinates of the center of area of the FOV (m)

**Results and Discussion.** A comparison of velocity magnitude between measurements and simulations in the Y-plane is shown in Fig. 4.34 for the first transient case. The experimental contours are ensemble averages of 321 cycles. Also, the plots at certain locations are shown for quantitative comparison. The flow field before the SOI shows an anticlockwise tumble vortex in both experiments and simulations. The vortex is more smeared out due to averaging of cycles with highly fluctuating velocities as seen from the plots at a location 10 mm downstream of the cylinder head. After SOI, the high-speed gas jet penetrates the tumble vortex destroying the overall tumble motion in the cylinder. As seen in the steady-state



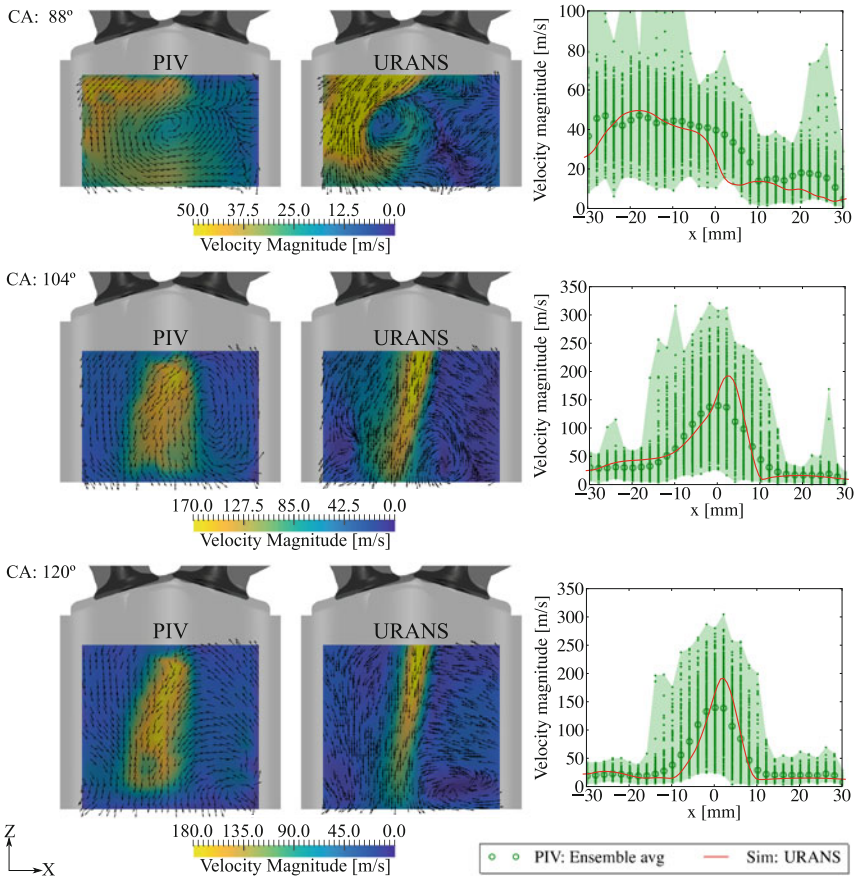


**Fig. 4.34** Contour plots for transient case 1: comparison of velocity magnitude, ensemble-averaged PIV (left) and URANS (right) in  $Y = 0.0$  plane at a crank angle  $88^\circ$  (before SOI),  $104^\circ$ , and  $120^\circ$  ATDC (after SOI); line plots: CA  $88^\circ$ — $Z = -10$  mm, CA  $104^\circ$ — $Z = -15$  mm, CA  $120^\circ$ — $Z = -15$  mm

configuration, the gas jet is highly fluctuating due to the complex interaction of the flow field and shocks/discontinuities and their reflections from the walls of the combustion chamber resulting in high variability in the experimental data ranging, for example, from 25 to 310 m/s. Nevertheless, the URANS simulations reasonably capture the ensemble-averaged velocity magnitude.

The tumble number comparison between the simulations and experiments provides an integral validation over a range of crank angles. In the experiments, the field of view (FOV) is limited due to practical limitations. Therefore, in both simulations and experiments, the planar tumble number is calculated using the velocity field in the same FOV (see Fig. 4.35a). The comparison between the

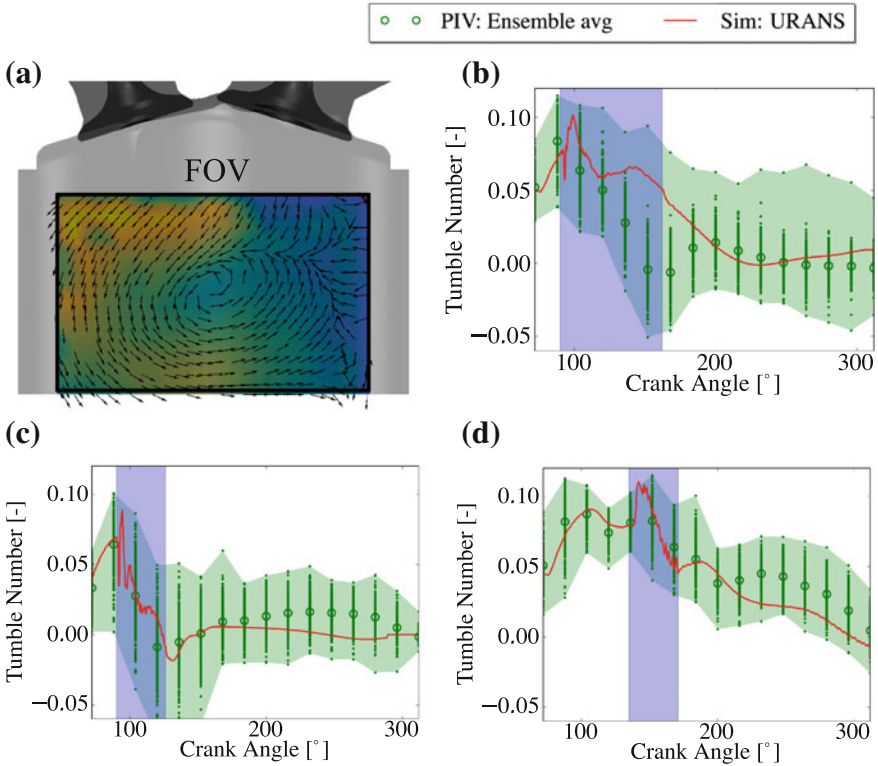


**Fig. 4.35** a Field of view for the calculation of tumble number; Comparison of tumble number in  $Y = 0.0$  plane for transient cases with **b** 2000 RPM-15 bar, **c** 1000 RPM-15 bar, **d** 2000 RPM-8 bar (injection period is indicated by vertical shaded region)

tumble number from URANS simulations and ensemble-averaged tumble number from PIV experiments for all transient cases (Fig. 4.35b, c, d) is reasonable despite the restrictive FOV. As a common observation, the tumble number decreases sharply after the injection starts, which is consistent with the observations made from contour plots, i.e., destruction of tumble vortex by the gas jet. Depending on the DOI, SOI, and injection pressure, the tumble vortex is destroyed either completely as in transient case 1 and 2 or partly as in transient case 3. With lower injection pressure in case 3, the mass flow rate is lower, reducing the overall momentum of the gas jet. In this case, the tumble vortex partly survives due to lower momentum combined with shorter duration of injection.

Thus, the MBC model for poppet-type injectors has been successfully validated against the in-cylinder PIV measurements. The model reduced the simulation run-times for full engine cycle with injection from the order of months to the order of weeks on the same computational resource, at the same time ensuring the reasonable accuracy of the predicted results.

## 4.5 Impact of Direct Gas Injection on the In-Cylinder Flow Field and Mixing

After the validation of the full engine simulation data, the impact of direct gas injection on the in-cylinder flow field is investigated using integral quantities such as mass-averaged tumble number and mass-averaged TKE. The mass-averaged quantities provide more information than the plane-averaged quantities, which were available in the experiments. Without direct gas injection, the mass-averaged tumble number follows an M-shape behavior, which is typical for spark-ignition (SI) engines (see Fig. 4.36a). On the other hand, with gas injection, the tumble number drops sharply for the cases with higher injection pressure. For the case with lower injection pressure, some of the tumble motion still survives because of the lower momentum of the gas jet. For the same injection pressure of 15 bar, the rate of decrease of the tumble number in a crank angle space is higher for lower engine speed. This is because the absolute in-cylinder flow velocities are lower for lower engine speed, and the gas jet has more time to interact with the tumble vortex.

The in-cylinder tumble flow has a special significance for SI engines (Arcoumanis et al. 1990; He et al. 2007). The tumble vortex is intentionally generated in the cylinder and acts as a storage of kinetic energy. The piston motion compresses the vortex as it moves toward TDC, which increases its angular speed (spin-up effect). Close to firing TDC, the tumble vortex breaks up releasing the kinetic energy in the form of turbulence, which is required for faster flame propagation. Figure 4.36b shows the mass-averaged TKE for the simulations considered here. As expected, without injection, the TKE levels are higher for higher engine speed. However, during the injection, the gas jet introduces very high amounts of TKE until the end of injection (EOI), which is the result of high velocities of the jet as well as the destruction of the tumble vortex. The highest maximum TKE is

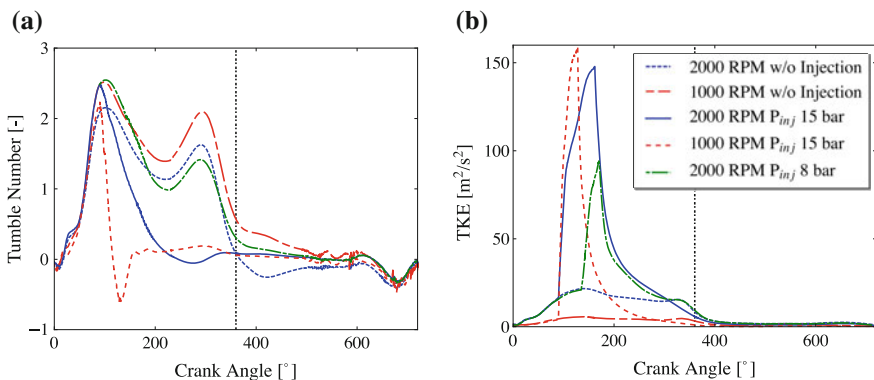


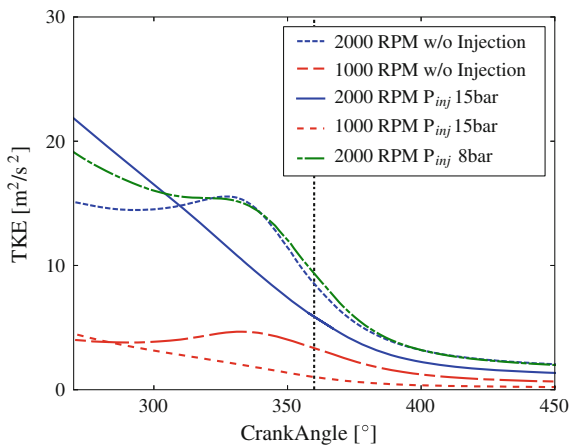
**Fig. 4.36** Comparison of the in-cylinder mass-averaged tumble number (a) and mass-averaged TKE (b) without injection (*fourth engine cycle*) and with injection (*fifth engine cycle*) for two injection pressures (vertical dashed lines indicate the crank angle of firing TDC)

observed for the case with high injection pressure and low engine speed. The maximum TKE is the lowest for low injection pressure and high engine speed among the considered cases. In this case, the surviving tumble vortex breaks up near firing TDC, resulting in the late increase in the TKE. Once the injection has ended, the TKE shows exponential decay as there is no production mechanism left in the absence of tumble motion, except the case with high engine speed and low injection pressure. The amount of TKE available near the firing TDC can be closely examined from Fig. 4.37. Except for 2000 RPM-8 bar case, the direct gas injection results in lower TKE levels than without injection. One of the major reasons for this is the centrally mounted injector configuration. If the injector is side-mounted or inclined in an angle that results in the gas jet assisting the in-cylinder tumble motion, the turbulence levels may be maintained or even be higher than without injection. Therefore, it is imperative to investigate the influence of direct gas injection on the in-cylinder flow and then optimize the injector configuration to obtain the desired turbulence levels for faster combustion.

High turbulence levels due to direct injection have a strong impact on the in-cylinder mixing. The mixture quality in the full engine case can be well described by the normalized cumulative volume fraction (CVF) of the injected gas. An ideal mixture is defined as a mixture with a constant mass fraction of the injected gas throughout the cylinder. The CVF is computed by adding the cylinder volume up to a certain mass fraction, which results in a monotonically increasing curve as shown in Fig. 4.38a. The ideal mixture is represented by a vertical line. The mixture quality for all the cases at firing TDC deviates from the ideal one. To quantify the deviation, more statistical information can be obtained from the CVF. A PDF is derived from the CVF (see Fig. 4.38b), and the mean, standard deviation, coefficient of variation, and skewness of the PDF are calculated.

Table 4.5 shows the statistical parameters computed for the mixture at firing TDC. The ideal mass fraction is computed from the total injected mass of helium divided by the total cylinder mass after the intake valve closing (IVC). The mean

**Fig. 4.37** Comparison of the in-cylinder mass-averaged TKE with and without injection at two injection pressures near firing TDC (vertical dashed line denotes the crank angle of firing TDC)



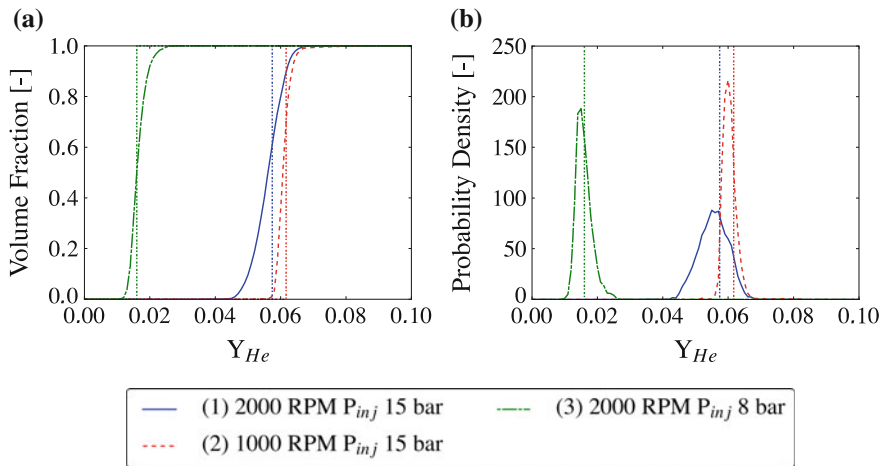


**Fig. 4.38** Mixture quality in terms of CDFs (a) and PDFs (b) at firing TDC for three cases (vertical dashed lines correspond to the mass fraction in case of ideal mixing)

**Table 4.5** Statistical parameters computed from the PDFs for three transient cases at firing TDC

Transient case	Ideal $Y_{He}$	Mean	Standard deviation	Coefficient of variation (%)	Skewness
1	0.05742	0.05554	0.004497	8.10	-0.05627
2	0.06170	0.06044	0.002305	3.81	2.3143
3	0.01592	0.01589	0.0024795	15.6	0.90298

values of the PDFs are lower than the ideal mass fraction because some of the injected helium is transported in the intake port before IVC. The standard deviation quantifies the degree of mixing. However, the standard deviation relative to the mean value, also known as the coefficient of variation (CoV), is more useful to compare mixture quality under different conditions. The lower the CoV, the higher the mixture quality. Case 2 with high injection pressure and low engine speed has the lowest CoV of helium mass fraction and hence the highest mixture quality. Case 3 with low injection pressure and high engine speed has a standard deviation similar to that of case 2; however, it has the lowest mixture quality, although visually the mixture looks more homogeneous (see Fig. 4.39). The mixture quality of the transient case correlates with the peak turbulence levels. Higher peak TKE is accompanied by a higher degree of mixing. A high positive skewness combined with a low CoV of the mass fraction implies that the volume contains pockets of a rich mass fraction, which can also be observed in the contour plots. The negative skewness in case 1 indicates the presence of regions with lean mass fractions, which can also be verified from the contour plots.

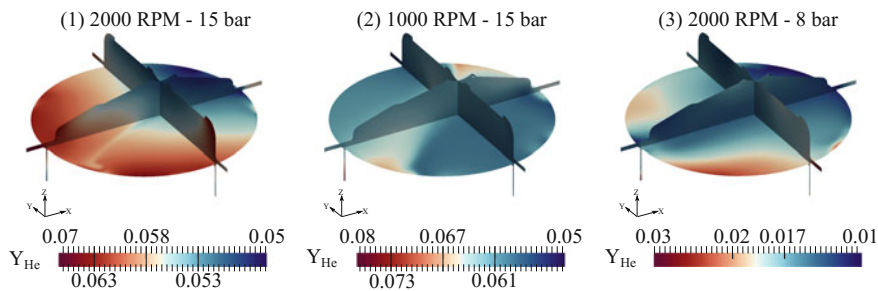


**Fig. 4.39** Helium mass fraction at firing TDC in three cases

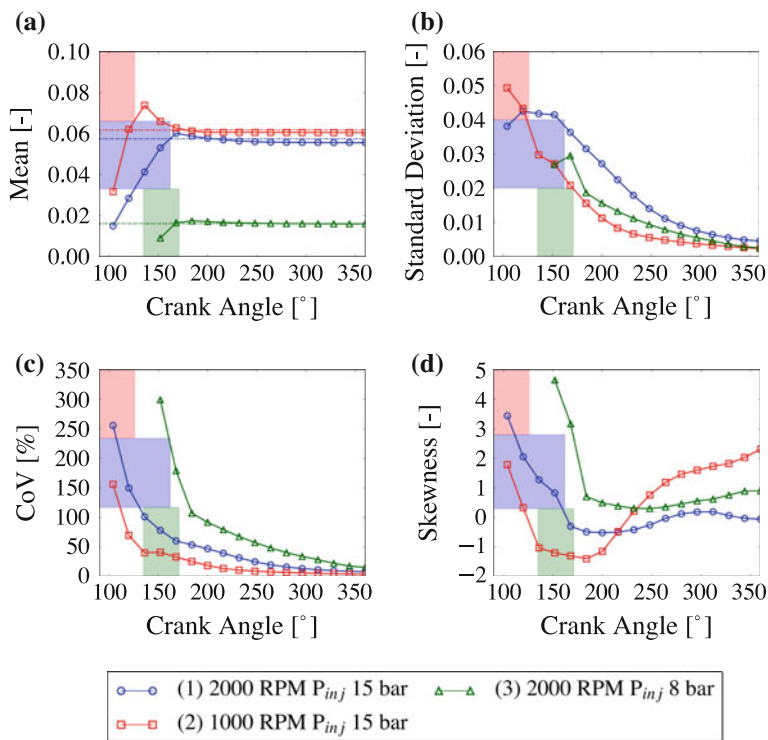


**Fig. 4.40** Evolution of mixing statistics over a crank angle (*filled regions indicate injection period for the respective cases, and horizontal dashed lines correspond to the ideal mass fraction after IVC*)

The mixing statistics can be tracked over a crank angle to assess the progress of mixing through the engine cycle (see Fig. 4.40). The mean of the PDFs increases during the injection and, after the EOI, approaches a constant value, which is close to the ideal one. All three cases have a high positive skewness at the beginning,

which is expected as the gas jet with rich helium mass fraction is concentrated in a very small region near the injection boundary. The skewness fluctuates throughout the mixing process and can be regarded as an indicator of the presence of rich or lean unmixed regions.

## 4.6 Summary

This chapter focuses on resolved simulations and modeling of poppet-type injectors and the potential impact of the direct gas injection on mixing and combustion. The resolved simulations of the poppet-type injector were performed using a high-fidelity LES solver, which provided detailed physical insights into the nozzle flow, near-nozzle flow, and the global hollow-cone jet characteristics. Specifically, complex gas passages in the injector nozzle lead to compression shocks and expansion fans causing a flow separation at the nozzle exit. The near-nozzle gas jet at steady state is inclined toward the poppet due to locally low pressure. The jet core remains intact despite the high standard deviation of the velocity field. Two distinct mixing layers develop on the inner and outer edge of the hollow cone and merge away from the nozzle. On the macroscopic level, the gas jet develops in two stages. The first stage involves the formation of a hollow cone, which then collapses and forms a single gas jet in the second stage. Turbulence models in URANS simulations are evaluated against the LES data, and it is found that the RNG  $k-\varepsilon$  model is suitable for the URANS simulations with respect to global characteristics and mixing behavior, which are important for general engine simulations. Therefore, it may be recommended for use in engine simulations with direct gas injection.

Injector needle motion essentially needs to be considered for resolved simulations of electromagnetically actuated solenoid injectors. The gradual opening of the needle results in a linear increase of axial penetration during the initial phase as observed in the experiments. Initial conditions in the injector may influence the global gas jet evolution and subsequent mixing. In the URANS simulations, different initial conditions lead to different collapsing instants, eventually affecting the overall development of the jet. However, the sensitivity to the initial conditions in the LES simulations is less prominent.

As the full engine simulations with detailed injector geometries are computationally expensive, the development of models for poppet-type injectors is necessary. However, there are currently only a few modeling approaches for such injectors in the literature. The recently developed MBC model considers the full geometry of the injector nozzle and is accurate. It is validated with PIV measurements in a steady-state flow configuration and full-cycle engine cases. URANS simulations and LES with MBC model for the injector predict similar levels of velocity magnitudes in *quasi*-steady-state simulations, although the LES also predicts highly fluctuating and dynamic interaction with the surrounding flow field. In the engine configuration, there is a reasonable agreement between the velocity field in URANS simulations and the ensemble-averaged velocity field in PIV

measurements. The MBC model reduced the simulation run-time to the order of weeks while enabling reasonably accurate simulations for further design and analysis.

Using the URANS simulation data, the impact of the gas jet on the in-cylinder flow field and mixing is analyzed. The direct gas injection introduces high turbulence in the cylinder potentially destroying the tumble vortex. High injection pressure at lower engine speeds results in high amounts of TKE because the high momentum of the gas jet breaks the weaker tumble motion at lower engine speeds. The TKE levels dissipate rapidly and may result in overall lower values with injection than without. The lower TKE values near firing TDC may lead to slower combustion if the engine is fired. Therefore, analysis of the DI-injector configuration must be performed, and ways to assist the tumble motion and maintain high turbulence levels until firing TDC must be investigated. The mixture quality is quantified by statistical parameters such as mean, standard deviation, CoV, and skewness of the PDFs derived from the CVFs of the in-cylinder mixture. As expected, higher TKE leads to lower CoV of the PDFs indicating a higher degree of mixing among the considered cases.

## 4.7 Future Work and Challenges

In the future, high-fidelity simulations with the LES approach including needle motion are required to verify the conclusions of the URANS approach and accurately predict the initial stages of the hollow-cone gas jet formation. The sensitivities of the URANS simulations to the initial conditions in the nozzle need to be scrutinized. To resolve the near-nozzle supersonic jet features in detail and investigate resulting instabilities, a higher mesh resolution is required.

The MBC model has some limitations. The inflow profiles are generated for a given pressure ratio across the nozzle and, for the cases considered in this chapter, the nozzle pressure ratio does not change significantly, as the injection occurs during the intake stroke. However, the nozzle pressure ratio may change depending on the SOI if the cylinder pressure fluctuates during the engine cycle, particularly at high engine speeds. In such cases, the nozzle may operate in under-expanded, perfectly expanded, overexpanded, or subsonic regimes, which will require dynamic mapping of inflow profiles, which is currently challenging. Additionally, the mesh resolution at the mapping boundary needs to be high enough to map the highly accurate boundary conditions from the nozzle flow simulation and obtain reasonably accurate in-cylinder flow fields. This has direct implications on the possibilities of further reduction of the simulation run-times.

**Acknowledgements** This work was performed within the Ford RWTH-Aachen Research Alliance Project FA-0099 funded by the Ford Motor Company. The authors would like to thank Delphi Automotive PLC for providing the injector and the appropriate control unit for the experimental measurements. The authors gratefully acknowledge the support and computing



resources provided by JARA-HPC partition of RWTH Compute Cluster under project JARA0117. The authors would like to thank Cascade Technologies Inc. for providing the license for the compressible LES solver CHRIS. The authors are also thankful to Convergent Science Inc. for providing the license for CONVERGE and support during the project.

## References

- ANSYS® Meshing (Release 15.0) (2013) Computer Software. ANSYS, Inc., Canonsburg, PA
- Arcoumanis C, Hu Z, Vafidis C, Whitelaw J (1990) Tumbling motion: a mechanism for turbulence enhancement in spark-ignition engines. SAE technical paper 900060. <https://doi.org/10.4271/900060>
- Baratta M, Catania AE, Pesce FC (2011) Multidimensional modeling of natural gas jet and mixture formation in direct injection spark ignition engines—development and validation of a virtual injector model. *ASME J Fluids Eng* 133(4):041304–041304-14. <https://doi.org/10.1115/1.4003877>
- Baratta M, Misul D, Xu J, Fuerhapter A et al (2017) Development of a high performance natural gas engine with direct gas injection and variable valve actuation. *SAE Int J Engines* 10 (5):2535–2551
- Bartolucci L, Scarcelli R, Wallner T, Swantek A et al (2016) CFD and X-ray analysis of gaseous direct injection from an outward opening injector. SAE technical paper 2016-01-0850. <https://doi.org/10.4271/2016-01-0850>
- Brès G, Ham F, Le H, Shoeybi M (2012) User's and developer's manual. Jefferson Release Version 4.0.4
- Chiodi M, Berner H, Bargende M (2006) Investigation on different injection strategies in a direct-injected turbocharged CNG-engine. SAE technical paper 2006-01-3000. <https://doi.org/10.4271/2006-01-3000>
- Deshmukh AY, Mayer D, Bode M, Falkenstein T et al (2016) LES of direct gas injection in internal combustion engines. Presented at LES for internal combustion engine flows LES4ICE, France, Nov 30–Dec 1, 2016
- Deshmukh A, Vishwanathan G, Bode M, Pitsch H et al (2018a) Characterization of hollow cone gas jets in the context of direct gas injection in internal combustion engines. SAE technical paper 2018-01-0296. <https://doi.org/10.4271/2018-01-0296>
- Deshmukh A, Vishwanathan G, Bode M, Pitsch H et al (2018b) Characterization of hollow cone gas jets in the context of direct gas injection in internal combustion engines. *SAE Int J Fuels Lubr* (accepted 2018)
- Deshmukh A, Falkenstein T, Pitsch H, Khosravi M et al (2018c) Numerical investigation of direct gas injection in an optical internal combustion engine. SAE technical paper 2018-01-0171. <https://doi.org/10.4271/2018-01-0171>
- Eilts P (2016) Future of the internal combustion engine. *ATZoffhighway Worldwide* 9(3):50. <https://doi.org/10.1007/s41321-016-0524-8>
- European Council for Automotive R&D. EUCAR Project Book. [http://www.eucar.be/wp-content/uploads/2016/12/Projectbook\\_2017\\_WEB.pdf](http://www.eucar.be/wp-content/uploads/2016/12/Projectbook_2017_WEB.pdf). Accessed July 2018
- Farrace D, Panier R, Schmitt M, Boulouchos K et al (2015) Analysis of averaging methods for large eddy simulations of diesel sprays. *SAE Int J Fuels Lubr* 8(3):568–580. <https://doi.org/10.4271/2015-24-2464>
- Fuchs T, Rutland C (1998) Intake flow effects on combustion and emissions in a diesel engine. SAE technical paper 980508. <https://doi.org/10.4271/980508>
- He Y, Selamet A, Reese R, Vick R et al (2007) Impact of tumble on combustion in SI engines: correlation between flow and engine experiments. SAE technical paper 2007-01-4003. <https://doi.org/10.4271/2007-01-4003>

- Hirsch C (1994) Numerical computation of internal and external flows: volume 2: Computational methods for inviscid and viscous flows. Wiley, Chichester, pp 344–401. ISBN: 0471923516
- Husted H, Karl G, Schilling S, Weber C (2014) Direct injection of CNG for driving performance with low CO<sub>2</sub>. Presented at 23rd Aachen colloquium automobile and engine technology, Germany, 6–8 Oct 2014
- INGAS—Integrated GAS Powertrain. Project Final Report. [http://www.ingas-eu.org/docs/INGAS\\_PROJECT\\_FINAL\\_REPORT\\_31May2012.pdf](http://www.ingas-eu.org/docs/INGAS_PROJECT_FINAL_REPORT_31May2012.pdf). Accessed Sept 2017
- Jensen JE, Tuttle WA, Stewart RB, Brechna H et al (1980) Brookhaven National Laboratory selected cryogenic data notebook, vol 1, Sections 1–9, United States
- Johnson NL, Amsden AA, Naber JD, Siebers DL (1995) Three-dimensional computer modeling of hydrogen injection and combustion. Presented at '95 SMC simulation multiconference, Phoenix, Arizona, USA, 9–13 April 1995
- Keskinen K, Kaario O, Nuutinen M, Vuorinen V et al (2016) Mixture formation in a direct injection gas engine: numerical study on nozzle type, injection pressure and injection timing effects. *Energy* 94:542–556. <https://doi.org/10.1016/j.energy.2015.09.121>
- Khalighi Y, Ham F, Nichols J, Lele S et al (2011) Unstructured large eddy simulation for prediction of noise issued from turbulent jets in various configurations. In: 17th AIAA/CEAS aeroacoustics conference (32nd AIAA aeroacoustics conference), aeroacoustics conferences, Portland, Oregon. <https://doi.org/10.2514/6.2011-2886>
- Kim G, Kirkpatrick A, Mitchell C (2004) Computational modeling of natural gas injection in a large bore engine. *ASME J Eng Gas Turbines Power* 126(3):656–664. <https://doi.org/10.1115/1.1762906>
- Kim G, Kirkpatrick A, Mitchell C (2007) Supersonic virtual valve design for numerical simulation of a large-bore natural gas engine. *ASME J Eng Gas Turbines Power* 129(4):1065–1071. <https://doi.org/10.1115/1.2747251>
- Kuensch Z, Schlatter S, Keskinen K, Hulkkonen T et al (2014) Experimental investigation on the gas jet behavior for a hollow cone piezoelectric injector. SAE technical paper 2014-01-2749. <https://doi.org/10.4271/2014-01-2749>
- Mather DK, Reitz RD (2000) Modeling the effects of auxiliary gas injection on diesel engine combustion and emissions. SAE technical paper 2000-01-0657. <https://doi.org/10.4271/2000-01-0657>
- McCracken M, Abraham J (2001) Swirl-spray interactions in a diesel engine. SAE technical paper 2001-01-0996. <https://doi.org/10.4271/2001-01-0996>
- Menter FR (1994) Two-equation eddy-viscosity turbulence models for engineering applications. *AIAA J* 32(8):1598–1605. <https://doi.org/10.2514/3.12149>
- Müller F, Schmitt M, Wright Y, Boulouchos K (2013) Determination of supersonic inlet boundaries for gaseous engines based on detailed RANS and LES simulations. *SAE Int J Engines* 6(3):1532–1543. <https://doi.org/10.4271/2013-24-0004>
- Ouellette PP, Hill PG (1999) Turbulent transient gas injections. *ASME J Fluids Eng* 122(4):743–752. <https://doi.org/10.1115/1.1319845>
- Richards KJ, Senecal PK, Pomraning E (2016) CONVERGE (v2.3), Convergent Science, Madison, WI
- Sevik J, Pamminger M, Wallner T, Scarcelli R et al (2016) Influence of injector location on part-load performance characteristics of natural gas direct-injection in a spark ignition engine. *SAE Int J Engines* 9(4):2262–2271. <https://doi.org/10.4271/2016-01-2364>
- Shih TH, Liou WW, Shabbir A, Yang Z, Zhu J (1995) A new k- $\epsilon$  eddy viscosity model for high reynolds number turbulent flows. *Comput Fluids* 24(3):227–238. [https://doi.org/10.1016/0045-7930\(94\)00032-T](https://doi.org/10.1016/0045-7930(94)00032-T)
- Shu C-W, Osher S (1988) Efficient implementation of essentially non-oscillatory shock-capturing schemes. *J Comput Phys* 77(2):439–471. [https://doi.org/10.1016/0021-9991\(88\)90177-5](https://doi.org/10.1016/0021-9991(88)90177-5)
- Sukumaran S (2010) Numerical study on mixture formation characteristics in a direct-injection hydrogen engine. Master thesis, Mechanical Engineering Department, Iowa State University, Ames, Iowa

- Van Sciver SW (2012) Helium cryogenics. International cryogenics monograph series. Springer Science+Business Media, LLC. <https://doi.org/10.1007/978-1-4419-9979-5>
- Vreman B, Geurts B, Kuerten H (1995) Subgrid-modelling in LES of compressible flow. *Appl Sci Res* 54(3):191–203. <https://doi.org/10.1007/BF00849116>
- Vuorinen V, Wehrfritz A, Duwig C, Boersma BJ (2014) Large-eddy simulation on the effect of injection pressure and density on fuel jet mixing in gas engines. *Fuel* 130:241–250. <https://doi.org/10.1016/j.fuel.2014.04.045>
- Wilson KG (1983) The renormalization group and critical phenomena. *Rev Mod Phys* 55(3):583–600. <https://doi.org/10.1103/RevModPhys.55.583>
- Yakhot V, Orszag SA (1986) Renormalization group analysis of turbulence. I. Basic theory. *J Sci Comput* 1(1):3–51. <https://doi.org/10.1007/BF01061452>